**RESEARCH ARTICLE**

# A Practical Approach to FMCW Radar Deconvolution in the Sea Ice Domain

THOMAS NEWMAN [1], JULIENNE C. STROEVE [2,3,4], VISHNU NANDAN [5],
ROSEMARY C. WILLATT [1], JAMES B. MEAD[6], (Senior Member, IEEE), ROBBIE MALLETT [7],
MICHEL TSAMADOS [1], MARCUS HUNTEMANN[8], STEFAN HENDRICKS [3],
GUNNAR SPREEN [8], AND RASMUS T. TONBOE [9]

[1]Centre for Polar Observation and Modelling, Earth Sciences, University College London, WC1E 6BT London, U.K.
[2]Centre for Earth Observation Science, University of Manitoba, Winnipeg, MB R3T 5V6, Canada
[3]Alfred Wegener Institute, Helmholtz Centre for Polar and Marine Research, 27570 Bremerhaven, Germany
[4]National Snow and Ice Data Center, University of Colorado, Boulder, CO 80918, USA
[5]Department of Electronics and Communication Engineering, Amrita Vishwa Vidyapeetham, Bengaluru Campus, Bengaluru, Karnataka 560035, India
[6]ProSensing, Amherst, MA 01002, USA
[7]Department of Physics and Technology, UiT The Arctic University of Norway, 9019 Tromsø, Norway
[8]Institute of Environmental Physics, University of Bremen, 28359 Bremen, Germany
[9]Department of Space Research and Technology, Technical University of Denmark, 2800 Lyngby, Denmark

Corresponding author: Thomas Newman (t.newman@ucl.ac.uk)

**ABSTRACT** This paper presents a practical step-by-step approach to Frequency Modulated Continuous Wave (FMCW) radar nonlinearity correction (deconvolution), utilizing surface-based Ku- and Ka-band radar data collected over nilas ice within a newly-opened sea ice lead during the 2019/2020 MOSAiC expedition. Two performance metrics are introduced to evaluate deconvolution effectiveness: the spurious free dynamic range (SFDR), which quantifies sidelobe suppression, and the leading edge width (LEW), which quantifies the improvement in surface return clarity. The impact of deconvolution waveforms on different survey dates, radar polarizations, and surface types is examined using echograms and quantitative metrics. Deconvolution results in a maximum SFDR increase of 28 dB, with a maximum 3 dB decline in deconvolution performance observed over an 8-day period and a maximum decline of 15 dB observed over a 71-day period. The LEW values indicate that the effectiveness of deconvolution in enhancing interface clarity depends on the combination of pre-deconvolution sidelobe shape, prominence of the surface return, the influence of snowpack returns, as well as a time-dependent reduction in deconvolution performance. Deconvolution significantly improves surface return clarity for cross-polarized radar data, where weak surface returns are obscured by returns from within the snowpack. The results demonstrate that deconvolution performance is most effective shortly after deconvolution waveform characterization. Therefore, it is recommended to

The associate editor coordinating the review of this manuscript and approving it for publication was Cheng Hu [].

perform at least weekly calibrations using a large metal sheet and ideally calibration before/after data collection to ensure optimal deconvolution performance and effective sidelobe suppression.

**INDEX TERMS** Arctic, deconvolution, frequency modulated continuous wave (FMCW), MOSAiC expedition, nonlinearity correction, polarimetry, radar, sea ice, snow, surface-based radar.

## I. INTRODUCTION

The polar regions are currently experiencing some of the most rapid changes on the planet. In recent decades, the Arctic has warmed at a rate nearly four times higher than the global average [2]; resulting in significant reductions in sea ice cover, the increased melting of the Greenland ice sheet and other ice caps and glaciers, a decrease in snow cover duration and amount, and the thawing of permafrost. The warming of the Antarctic Peninsula has been more pronounced than in any other landmass in the Southern Hemisphere, leading to the destabilization of floating ice shelves and the disruption of ecosystems [3].

Due to the harsh and remote nature of polar regions, satellite remote sensing techniques have provided crucial insights into environmental changes occurring there. Radar-based satellite sensors are particularly effective in these regions as they can penetrate clouds and operate during polar night. These sensors include radar altimeters such as CryoSat-2 [4], AltiKa [5], and Sentinel-3 [6]; scatterometers such as ASCAT-B/C, OSCAT, and HY-2A [7]; and Synthetic Aperture Radars (SAR) such as RADARSAT-2, Sentinel-1A/B, TerraSAR-X, and ALOS-2/PALSAR-2 [8], [9].

While satellite observations offer wide coverage of the polar regions, airborne and surface-based sensors have played a vital role in improving our understanding of radar interactions with frozen surfaces, thanks to their smaller footprints, less ambiguous surface returns and clearer relationship to coincident geophysical data such as snow depth, density etc.

Frequency Modulated Continuous Wave (FMCW) radar systems have gained significant popularity in Cryospheric research. Compared to traditional pulsed radar systems, FMCW radars offer several key advantages: such as fine range resolution (over short-range windows), and the ability to operate at very small target ranges. The fine range resolution of FMCW radar systems is achieved through their large pulse compression ratios, which also allows for reduced transmitted peak powers. Additionally, the mixing operation central to FMCW radar processing allows for relatively low sampling frequencies, which, combined with their lower power requirements, makes FMCW considerably less expensive than comparable pulsed radar systems [10], [11], [12].

FMCW radars have been used extensively in surface-based applications [13], [14], [15] and airborne campaigns [16], [17], [18], including NASA's Operation IceBridge [19], [20], [21], [22], [23], [24]. Recently, the surface-based dual-frequency Ku- and Ka-band fully polarimetric radar (KuKa) was developed to investigate the scattering properties of the sea ice snowpack. KuKa, deployed during the year-long Multidisciplinary drifting Observatory for the Study of Arctic Climate (MOSAiC) expedition [25], functions as both an altimeter (stare mode) and a scatterometer (scan mode). Its aim during the MOSAiC campaign was to investigate the seasonal evolution of snow over sea ice and its impact on the dominant scattering surface [26], [27].

Although FMCW radar has become a powerful tool for remote sensing applications, deviations from ideal linear FM modulation make it susceptible to various sources of signal distortion and interference, which can compromise the accuracy and reliability of the collected data. One critical factor contributing to data quality degradation is the presence of range sidelobes [28], [29], [30], caused by amplitude and phase nonlinearities in the linear FM modulation [31], [32], [33], [34]. In radar remote sensing, range sidelobes appear as weaker signals that closely mirror the primary surface return; potentially obscuring interfaces, and leading to incorrect geophysical interpretations [22], [23], [35], [36]. The KuKa radar system deployed during the MOSAiC expedition encountered similar issues with range sidelobes: degrading data quality and obscuring interface returns [26].

Nonlinearity correction methods for FMCW radar have been developed to suppress range sidelobes and improve the clarity of surface returns. The literature proposes two general strategies to characterize and correct deviations in amplitude and phase from ideal linear FM modulation: hardware correction methods, which are applied during signal generation, and software correction methods, which are applied during post-processing. For the remainder of this paper, we will use the shorter term *deconvolution* to refer to software nonlinearity correction methods that are applied during post-processing.

In sea ice remote sensing, deconvolution methods –also commonly known as system response deconvolution– have been successfully applied to data collected during airborne sea ice campaigns [19], [22], [23], [37]. In these deployments, the characteristics of range sidelobes have been observed to vary between different field campaigns, adding multi-seasonal complexity to data interpretation. Deconvolution effectively suppresses range sidelobes, making the data more consistent across seasons. This allows for more accurate interpretation of sea ice scattering physics and enables interface-tracking algorithms to be applied more reliably to data from different campaigns [22].

The primary objective of this paper is to provide a practical guide to FMCW radar deconvolution. It specifically focuses on the KuKa surface-based FMCW radar system and includes instructions on how to generate deconvolution waveforms

from radar impulse responses obtained from calibration datasets commonly found in the sea ice domain, such as newly-opened leads. Additionally, the paper introduces performance metrics that can be used to quantify the effectiveness of deconvolution techniques.

The remainder of this paper is organized as follows. Section II provides a brief overview of the principles of FMCW radar, describes the origins of FMCW radar nonlinearities, and explains the application of FMCW radar deconvolution in the literature. In Section III, we give a concise overview of the KuKa radar hardware and describe how the data were acquired during the MOSAiC expedition. We also discuss the KuKa calibration experiments conducted during MOSAiC and the utilization of newly-opened leads to obtain the radar impulse response. Section IV outlines the processing steps required to generate deconvolution waveforms using the impulse response data collected during the KuKa lead transects. These deconvolution waveforms can be applied to the entire KuKa MOSAiC dataset to suppress sidelobes and enhance data quality. In Section V, we present the results of the deconvolution process, assessing its effectiveness by analyzing KuKa data from three different survey dates. We use an echogram from each survey to provide a qualitative description of deconvolution effectiveness, while a waveform from each echogram is used to provide a quantitative assessment. In Section VI, we discuss how the surface type affects the radar return and the features that become visible after deconvolution. We also utilize various performance metrics to quantify the changes in deconvolution performance over time and evaluate the impact of deconvolution on improving surface return clarity. Section VII provides a summary of our findings and discusses potential future research directions.

## II. BACKGROUND
In this background section, we provide a brief overview of the principles and key equations that govern FMCW radar, describe the origins of FMCW radar nonlinearities, and finally explain how FMCW radar deconvolution is applied in the literature.

### A. THE FMCW OPERATING PRINCIPLES
FMCW radar systems commonly transmit chirp waveforms that have a constant amplitude and a linear variation in frequency with time (i.e. a quadratic variation in phase with time) [10], [11], [12]. Chirp waveforms are designed to sweep through bandwidth, $B$, over sweep duration, $T_s$, and have a frequency sweep rate, $K$, that is given by,

$$K = \frac{B}{T_s} \qquad (1)$$

For a complex chirp signal, the instantaneous frequency, $f_i$, at any time, $t$, within the sweep, defines the rotation rate of a phasor that is given by,

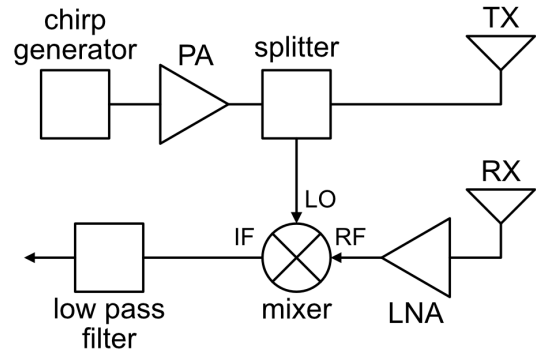$$f_i(t) = \frac{d\phi(t)}{dt} = f_0 + Kt \qquad (2)$$



**FIGURE 1.** Diagram showing a simplified FMCW radar system. PA is the Power Amplifier, LNA is the low-noise amplifier, TX is the transmit antenna, RX is the receive antenna; LO, RF, and IF, correspond to the local oscillator, radio frequency, and intermediate frequency mixer ports, respectively.

where, $\phi(t)$ is the signal phase, $f_0$ is the frequency at time $t = 0$, and $f_1$ is the frequency at time $t = T_s$.

A diagram showing a simplified FMCW radar, employing a two-antenna homodyne architecture [38], is presented in Fig. 1. A chirp signal is produced in the chirp generator i.e. a Voltage-Controlled Oscillator (VCO) [32] or a digital linear FM synthesizer [39], [40]. The chirp signal is first amplified by a Power Amplifier (PA), before being sent into a power divider (splitter), the signal then takes two separate paths. One copy of the chirp signal is sent directly into the Local Oscillator (LO) port of the mixer; we designate this as $S_{LO}$. The other copy of the chirp signal is passed to the transmit antenna (Tx antenna) and is subsequently radiated into the antenna Field Of View (FOV); after a range-dependent delay, reflections from objects within the FOV are collected by the receive antenna (Rx antenna), are then amplified by a low-noise amplifier (LNA), before being directed into the Radio frequency (RF) port of the mixer; we designate this signal as $S_{RF}$. The mixer will combine $S_{LO}$ and $S_{RF}$ to produce an output intermediate frequency (IF) signal, $S_{IF}$, which is subsequently low pass filtered to remove the high-frequency components (that are not part of the desired signal) to obtain the *beat signal $S_b$*. The mixing and low pass filtering operation down-converts the incoming received signals to baseband; allowing FMCW radars to operate at much lower sampling frequencies than equivalent pulsed radar systems [11], [12].

### B. TRANSMIT AND RECEIVE SIGNALS
For an FMCW radar system, $S_{LO}$, can be expressed mathematically, as,

$$S_{LO}(t) = A_{LO}(t) \cdot \exp\{i [\phi_{LO}(t)]\} \qquad (3)$$

where $A_{LO}(t)$ is the amplitude of $S_{LO}$, and $\phi_{LO}(t)$ is the phase of $S_{LO}$ (obtained via the integral of (2)), and given by,

$$\phi_{LO}(t) = 2\pi \left[ f_0 t + \frac{1}{2} K t^2 \right] \qquad (4)$$

For a theoretical system $A_{LO}(t)$ will be time invariant (have a constant amplitude) across its entire bandwidth, with $\phi_{LO}(t)$ having a perfectly quadratic variation of phase with time (a linear variation in frequency with time).

In the theoretical case, an echo from a single point target in the antenna FOV will be an exact replica of the transmitted chirp, but delayed by the two-way travel time, $\tau$, given by,

$$\tau = \frac{2R}{c} \tag{5}$$

where, $R$ is the range to the target, and $c$ is the speed of light. We can modify (3) to give an expression for $S_{RF}$, given as,

$$S_{RF}(t, \tau) = A_{RF}(t, \tau) \cdot \exp\{i[\phi_{RF}(t, \tau)]\} \tag{6}$$

where, $A_{RF}(t, \tau)$ is the amplitude of $S_{RF}$; which takes into account factors such as Tx and Rx antenna gains, spherical spreading, target reflectivity and LNA gain. The term $\phi_{RF}(t, \tau)$ is the phase of $S_{RF}(t, \tau)$, which is assumed, again, to be a perfectly quadratic variation of phase with time, given by,

$$\phi_{RF}(t, \tau) = 2\pi\left[f_0(t - \tau) + \frac{1}{2}K(t - \tau)^2\right] \tag{7}$$

For the case of scattering from multiple targets, or from a distributed target (i.e. one comprised of multiple connected sub-targets at different ranges), the received signal will actually be formed from the linear superposition of received signals from all $N$ individual targets (within the antenna FOV) giving,

$$S_{RF}(t) = \sum_{n=1}^{N} A_{RF,n}(t, \tau_n) \cdot \exp\{i[\phi_{RF}(t, \tau_n)]\} \tag{8}$$

with $A_{RF,n}(t, \tau_n)$ denoting the received amplitude from the $n^{th}$ target, and $\phi_{RF}(t, \tau_n)$ denoting the received phase, given by,

$$\phi_{RF}(t, \tau_n) = 2\pi\left[f_0(t - \tau_n) + \frac{1}{2}K(t - \tau_n)^2\right] \tag{9}$$

where, $\tau_n = 2R_n/c$ is the two-way travel time of target $n$ at range $R_n$ [41].

### C. MIXING TO GET THE BEAT SIGNAL

In a homodyne FMCW radar, the mixing operation (Section II-A) produces, $S_{IF}$. This operation is performed via the instantaneous multiplication,

$$S_{IF}(t, \tau) = S_{RF}(t, \tau) S_{LO}(t)^* \tag{10}$$

where $*$ represents the complex conjugate. It is important to note that due to the two-way travel time, $\tau$, and the finite sweep duration, $T_s$, only the instantaneously overlapping parts of the two signals can be multiplied and go on to produce $S_{IF}$.

The multiplication in (10) produces both *sum frequencies* and *difference frequencies*. The sum frequencies ($f_{RF} + f_{LO}$) are not desired and are removed by lowpass filtering the output $S_{IF}$ signal (Fig. 1). The difference

frequencies ($f_{RF} - f_{LO}$) are the desired beat signal, $S_b$, component, and for the case of a single point target are given by,

$$S_b(t, \tau) = A_{RF}(t, \tau)A_{LO}(t) \\ \cdot \exp\{i[\phi_{RF}(t, \tau) - \phi_{LO}(t)]\} \tag{11}$$

or equivalently,

$$S_b(t, \tau) = A_{RF}(t, \tau)A_{LO}(t) \\ \cdot \exp\left\{i\left[2\pi\left(f_0\tau + Kt\tau - \frac{1}{2}K\tau^2\right)\right]\right\} \tag{12}$$

The mixing operation thus results in the overlapping portion of quadratic phase ramp of $S_{LO}(t)$ being subtracted from the quadratic phase ramp of $S_{RF}(t, \tau)$; resulting in a beat signal, $S_b$, that will have a linear phase ramp (i.e. has a constant frequency).

For the case of a single point target the beat signal is actually a sinusoid with a frequency given by $f_b = K\tau$, which is proportional to the two-way travel time to the target, $\tau$, through,

$$f_b = K\tau = \frac{B}{T_s}\frac{2R}{c} \tag{13}$$

Upon substitution, the target range, $R$, can therefore be expressed as

$$R = \frac{cf_b}{2K} = \frac{cf_bT_s}{2B} \tag{14}$$

establishing the common FMCW relationship between range and beat signal frequency [38].

For the case of multiple targets, or a distributed target, the beat signal is given by,

$$S_b(t) = \sum_{n=1}^{N} A_{RF,n}(t, \tau_n)A_{LO}(t) \\ \cdot \exp\left\{i\left[2\pi\left(f_0\tau_n + Kt\tau_n - \frac{1}{2}K\tau_n^2\right)\right]\right\} \tag{15}$$

which is the sum of the beat signals from all $n$ targets within the antenna FOV; with targets at greater ranges to the antenna having higher beat frequencies and targets that are closer having lower beat frequencies (14).

### D. RANGE ACCURACY, RESOLUTION AND RANGE BIN SPACING

For an FMCW radar system, a single point target is represented by a single beat signal frequency (Section II-C). The location of spectral peaks in the frequency domain, obtained via a Fast Fourier Transform (FFT), can thus be used (via (14)) to determine the range to different targets within the antenna FOV.

The *range accuracy* of a FMCW radar system can be defined as the uncertainty in the detected peak centroid location. The range accuracy is thus independent of peak width, and is primarily influenced by the signal-to-noise

ratio (SNR) of the detected signal, and the amount of signal averaging performed [42].

The *range resolution* can be defined as the minimum distance that two targets can be separated (along the radar's line of sight) before they become indistinguishable from each other. For an FMCW radar system, the range resolution, $\delta R$, is controlled by the width of the beat signal spectral peak (i.e. the frequency precision, $\delta f$). From the Fourier similarity (scaling) theorem, the spectral width of a signal is the inverse of the total measurement time, $T$, given as,

$$\delta f = \frac{1}{T} \qquad (16)$$

If we assume that the total measurement time is equal to the sweep duration, $T = T_s$, then upon substitution of (1) and (16) into (14) we obtain,

$$\delta R = \frac{c}{2K} \delta f = \frac{c}{2K} \frac{1}{T_s} = \frac{c}{2B} \qquad (17)$$

From (17) it is observed that range resolution is inversely proportional to the bandwidth [42].

The application of window functions designed for spectral sidelobe reduction have the effect of degrading the theoretical range resolution by a widening factor $\alpha$. The frequency precision after windowing is $\delta f = \alpha/T_s$, and the associated range resolution is given by,

$$\delta R = \frac{c}{2B} \cdot \alpha \qquad (18)$$

An example of this widening effect is observed during the application of a Hann (Hanning) window, here windowing reduces the highest relative sidelobe level from $-13$ dB (for the case of no windowing) to $-32$ dB; with an associated doubling of the null-to-null mainlobe width due to the widening factor (relative to no windowing) of $\alpha = 2$, this translates to a $-3$ dB widening factor of $\alpha_{-3dB} = 1.62$ (1.44/0.89) [43], [44].

For FMCW radar systems, the *range bin spacing* determines by how the beat signal is sampled in the frequency domain. Frequency domain samples are typically spaced at the inverse of the sweep duration, thus allowing the spectrum of the beat signal to be sampled at $2/T_s$; with the equivalent range bin spacing, $\Delta R$, given by,

$$\Delta R = \frac{c}{2B} \qquad (19)$$

The range bin spacing can be made finer by a process known as *zero padding*, which involves appending zeros to the end of the beat signal in the time domain before performing the FFT. As a result, the number of data points in the FFT increases, leading to a finer frequency resolution, and the more accurate localization of the beat signal peak [38], [45].

### E. PHASE NOISE
Phase noise in FMCW radar systems can be caused by power supply variability, mechanical/acoustic vibrations, the non-ideal performance of mixers and high power amplifiers, as well as thermal and flicker noise internal to the chirp generator [12], [46], [47], [48]. Mathematically, the origin of phase noise is random short-term phase fluctuations, known as *phase jitter*, which causes the deviation of a signal from a perfect sinusoid; or comparably the instantaneous deviation in the phase angle of a rotating phasor compared to where it should be at any given time (for an ideal chirp signal). Noise sources can also affect the instantaneous magnitude of the rotating phasor; however, many oscillators operate in a saturated state which limits the amplitude components of the noise, causing the phase fluctuations to dominate [12].

In the frequency domain, phase noise is observed to broaden the power spectrum arising from targets in the antenna FOV and manifests itself as noise sidebands that spread out from either side of the main beat signal peak (known as *spectral spreading*) [48], [49]. These sidebands decrease in power level with increasing offset frequency, and taper off to a constant value as frequency independent thermal noise begins to dominate at the higher frequencies. It is important to note that unlike other noise sources, phase noise scales with signal power; meaning that the SNR cannot be improved by simply increasing the signal power. Phase noise sidebands can also spread clutter energy into the frequency region occupied by a target, thus reducing the target's signal-to-clutter ratio; this is especially an issue for radar systems with high dynamic ranges, with spectral spreading causing the clutter-floor to increase around large targets making the detection of small targets impossible in regions of heavy clutter [11], [50].

### F. SPURIOUS SIGNALS
In addition to the random component of the signal, caused by flicker, thermal, and phase noise [11] there are also periodic/deterministic variations that give rise to what are known as *spurious signals*. In the frequency domain spurious signals manifest themselves as discrete frequency spikes (also known as spurs) in the spectrum. There are a number of different types of spurious signals arising from unwanted periodic signal variations including: internal reflections, harmonics, intermodulation products, and LO nonlinearities [12].

Internal reflections in a radar system arise due to unwanted interactions between various radar system components. One primary reason for these reflections is non-ideal impedance matching. When the impedance is not perfectly matched, some of the radar signal power is reflected back instead of being fully transmitted or received. A specific example of this phenomenon is the multiple reflections that can occur between the RF port of the receiver mixer and the LNA (Fig. 1). These reflections can lead to the appearance of spurious peaks at specific frequency offsets, with *S-parameters* (scattering parameters) commonly used to characterize and quantify these reflections and the overall behavior of RF components [51], [52], [53].

Harmonics result from the fact that real-world signals are not perfect sinusoids; in radar systems harmonics are

generated due to the distortion produced by non-linear system components. Signals in the frequency domain show up as a peak at the fundamental frequency together with a set of harmonics represented by discrete peaks, that usually decrease in amplitude with increasing frequency. A non-ideal periodic signal of frequency $f$, will have a first harmonic at $f$ (the fundamental frequency), the second harmonic at $2f$, the third harmonic at $3f$, and so on, all at integer multiples, $n$, of its fundamental frequency $f$ i.e. $f, 2f, 3f, \cdots, nf$ [45]. In the context of a radar return from a target, the fundamental frequency will correspond to the target return at range, $R$, so harmonics will show up as spurious signals at integer multiples of the target range (Section II-C).

Intermodulation products result from the non-linear performance of mixers. In the ideal case a mixer acts as a frequency multiplier and produces output frequencies that are the sum and difference of the two input frequencies $f_{RF} - f_{LO}$ and $f_{RF} + f_{LO}$ (Section II-C). In real operation mixers will also produce unwanted spurious signals at any frequency combinations of RF and LO signals $\pm m f_{LO} \pm n f_{RF}$ (where $m$ and $n$ are integers). When the combinations of these signals appear within the frequency range of interest they are known as in-band intermodulation products; these spurious signals are difficult to filter out and can degrade radar system performance [11].

### G. THE LEAKAGE SIGNAL

Spurious signals can occur even in the absence of a transmitted RF signal due to the direct leakage of residual LO signal between the different ports of a mixer (Fig. 1). Signal leakage is caused by finite port-to-port isolation, mismatches between receiver components, significant DC offset at the mixer output, power supply coupling, and parasitic capacitance [46], [54]. There are two common leakage pathways: LO feedthrough and reverse LO feedthrough. In LO feedthrough residual signal passes from the mixer's LO input port to the IF output port; this extra signal can potentially desensitize the receiver.

Reverse LO feedthrough is caused by residual LO signal being passed into the mixer's RF input port along with the original RF signal. This can occur due to: low isolation between the LO input port and the RF input port, residual LO signal leakage into the LNA, or the back reflection of signal from the antenna. The combined RF and residual LO signal is then mixed with the original LO signal, resulting in what is known as *self-mixing* [12], [54]. Self-mixing typically introduces a strong DC signal component at the IF output port, together with the generation of DC-centered phase noise sidebands which may mask weak signals at greater ranges [10], [49].

### H. FMCW NONLINEARITIES

In the idealized case, linear FMCW radar systems transmit chirp waveforms that have a constant amplitude and a perfectly quadratic variation of phase with time (linear variation in frequency with time) (Section II-B). In reality, residual amplitude and phase nonlinearities, in the chirp sweep, result in a degradation in radar system performance [10], [31], [39]. Nonlinearities can be caused by the nonlinear behaviour of the frequency synthesizer (that generates the chirp), as well as the non-ideal amplitude and phase performance (across the chirp sweep bandwidth) of radar system components [51], [52], [53], such as amplifiers, mixers, coaxial cables and antennas (Fig. 1). These nonlinearities represent another source of spurious signals, and are essentially time-independent, although there may be drifts that occur over larger timescales due to variations in temperature and power supply voltage [33], [34], [55].

We can modify (3) (the signal observed at the LO port of the mixer) to take into account the effects of the nonlinearities, to give,

$$S'_{LO}(t) = A'_{LO}(t) \cdot \exp\left\{i\left[\phi'_{LO}(t)\right]\right\} \tag{20}$$

where,

$$A'_{LO}(t) = A_{LO}(t) \cdot A_\varepsilon(t) \tag{21}$$
$$\phi'_{LO}(t) = \phi_{LO}(t) + \phi_\varepsilon(t) \tag{22}$$

here, $A_{LO}(t)$ and $\phi_{LO}(t)$ denotes the chirp amplitude and the chirp phase, respectively. The new terms $A_\varepsilon(t)$ and $\phi_\varepsilon(t)$ denote the amplitude and phase nonlinearities, respectively, of the signal observed at the LO mixer port.

We can, similarly, modify (6) (the signal observed at the RF port of the mixer) to take into account the nonlinearities, giving,

$$S'_{RF}(t, \tau) = A'_{RF}(t, \tau) \cdot \exp\left\{i\left[\phi'_{RF}(t, \tau)\right]\right\} \tag{23}$$

where,

$$A'_{RF}(t, \tau) = A_{RF}(t, \tau) \cdot A_\xi(t, \tau) \tag{24}$$
$$\phi'_{RF}(t, \tau) = \phi_{RF}(t, \tau) + \phi_\xi(t, \tau) \tag{25}$$

here, $A_{RF}(t, \tau)$ and $\phi_{RF}(t, \tau)$ denote the receive chirp amplitude and phase, respectively; and the new terms $A_\xi(t, \tau)$ and $\phi_\xi(t, \tau)$ denote the amplitude and phase nonlinearities, respectively, of the signal observed at the RF mixer port.

It is important to note that even for the case of a single point target with a (theoretical) zero range offset (i.e. $\tau = 0$), the nonlinearities at the RF and LO mixer ports will not be the same,

$$A_\xi(t, 0) \neq A_\varepsilon(t) \tag{26}$$
$$\phi_\xi(t, 0) \neq \phi_\varepsilon(t) \tag{27}$$

this is due to the fact that any amplitude and phase nonlinearities seen in $S'_{LO}(t)$ will be further modified by the non-linear characteristics of all the RF components along the RF path, i.e. Tx Antenna, Rx Antenna, LNA and coaxial cables (Fig. 1) [30].

In reality, we must incorporate the nonlinearities arising from all $N$ individual targets (or sub-targets of a distributed

target) within the antenna FOV, this requires a modification of (23) to give,

$$S'_{RF}(t) = \sum_{n=1}^{N} A'_{RF,n}(t, \tau_n) \cdot \exp\left\{i\left[\phi'_{RF,n}(t, \tau_n)\right]\right\} \quad (28)$$

where, $A'_{RF,n}(t, \tau_n)$ and $\phi'_{RF,n}(t, \tau_n)$ are the amplitude and phase contribution, respectively, of the *nth* target at a range of $R_n$, with the corresponding two-way travel time: $\tau_n = 2R_n/c$.

### I. BEAT SIGNAL NONLINEARITIES

It is important to note that as amplitude and phase nonlinearities are present in both $S'_{RF}(t, \tau)$ and $S'_{LO}(t)$, it is the relative time offset between the two signals (due to the two-way travel time, $\tau$) that will determine exactly how the nonlinearities combine to produce the signal observed at the IF mixer port, $S'_{IF}(t, \tau)$; given via (10), as,

$$S'_{IF}(t, \tau) = S'_{RF}(t, \tau)S'_{LO}(t)^* \quad (29)$$

Only the instantaneously overlapping parts of $S'_{RF}(t, \tau)$ and $S'_{LO}(t)$ are capable of being multiplied to produce $S'_{IF}(t, \tau)$.

Equation (11) can thus be modified to take into account the nonlinearities, to give,

$$\begin{aligned} S'_b(t, \tau) = &A'_{RF}(t, \tau) A'_{LO}(t) \\ &\cdot \exp\left\{i\left[\phi'_{RF}(t, \tau) - \phi'_{LO}(t)\right]\right\} \end{aligned} \quad (30)$$

or equivalently,

$$\begin{aligned} S'_b(t, \tau) = &\left[A_{RF}(t, \tau) \cdot A_\xi(t, \tau) \cdot A_{LO}(t) \cdot A_\varepsilon(t)\right] \\ &\cdot \exp\left\{i\left[\varphi(t, \tau) + \phi_\xi(t, \tau) - \phi_\varepsilon(t)\right]\right\} \end{aligned} \quad (31)$$

with the term $\varphi(t, \tau)$, given by,

$$\varphi(t, \tau) = 2\pi \left(f_0\tau + Kt\tau - \frac{1}{2}K\tau^2\right) \quad (32)$$

For the case of multiple targets, or a distributed target, (31) becomes,

$$\begin{aligned} S'_b(t) = \sum_{n=1}^{N} &\left[A_{RF,n}(t, \tau_n) \cdot A_{\xi,n}(t, \tau_n) \cdot A_{LO}(t) \cdot A_\varepsilon(t)\right] \\ &\cdot \exp\left\{i\left[\varphi(t, \tau_n) + \phi_{\xi,n}(t, \tau_n) - \phi_\varepsilon(t)\right]\right\} \end{aligned} \quad (33)$$

where, $A_{RF,n}(t, \tau_n), A_{\xi,n}(t, \tau_n)$, and $\phi_{\xi,n}(t, \tau_n)$ are the receive chirp amplitude, the amplitude nonlinearities, and the phase nonlinearities, respectively, from the *n'th* target; and where $\varphi(t, \tau_n)$ is given by,

$$\varphi(t, \tau_n) = 2\pi \left(f_0\tau_n + Kt\tau_n - \frac{1}{2}K\tau_n^2\right) \quad (34)$$

From (33) we see that the beat signal amplitude and phase are the result of the all $N$, targets within the antenna FOV.

### J. THE EFFECTS OF FMCW NONLINEARITIES

The amplitude of beat signal, $S'_b(t, \tau)$, can be defined as the multiple of all the amplitude terms in (31), giving,

$$A'_b(t, \tau) = A_C(t, \tau) \cdot A_\mathcal{E}(t, \tau) \quad (35)$$

where, we have combined the constant amplitude terms, as,

$$A_C(t, \tau) = A_{RF}(t, \tau) \cdot A_{LO}(t) \quad (36)$$

and the amplitude nonlinearities terms, as,

$$A_\mathcal{E}(t, \tau) = A_\xi(t, \tau) \cdot A_\varepsilon(t) \quad (37)$$

The value of amplitude term, $A_C(t, \tau)$, remains constant over the sweep duration, $T_s$, and is determined by the Tx and Rx antenna gains, spherical spreading, target reflectivity, LNA gains, and the original chirp amplitude. The value of the nonlinear amplitude term, $A_\mathcal{E}(t, \tau)$, varies over sweep duration and is caused by the nonlinear behavior of radar system components, and the frequency synthesizer.

The phase terms of the beat signal can be defined (via (31)), as,

$$\phi'_b(t, \tau) = \varphi(t, \tau) + \phi_\mathcal{E}(t, \tau) \quad (38)$$

where we have, similarly, combined the phase nonlinearities terms, as,

$$\phi_\mathcal{E}(t, \tau) = \phi_\xi(t, \tau) - \phi_\varepsilon(t) \quad (39)$$

here, the nonlinear phase term $\phi_\mathcal{E}(t, \tau)$ (also caused by the nonlinear behavior of radar system components, and the frequency synthesizer) appears superimposed upon the linear phase ramp (i.e. constant frequency) given by the $\varphi(t, \tau)$ term.

The presence of $A_\mathcal{E}(t, \tau)$ and $\phi_\mathcal{E}(t, \tau)$ results in amplitude and phase modulation, respectively, of the beat signal. The modulating effects of these nonlinearities will increase the spectral bandwidth of the target response, spreading target energy into different frequencies and away from the beat frequency. If the modulating effects are relatively small then the frequency domain representation of the beat signal will consist of a dominant peak (at the beat frequency) that will be broadened by the additional spectral content contained within $A_\mathcal{E}(t, \tau)$ and $\phi_\mathcal{E}(t, \tau)$; thus leading to coarser range resolution and a reduction in the SNR [28], [56].

The nonlinearities will also manifest themselves as discrete range sidelobes occurring on either side of the dominant beat signal peak; with the specific frequency content of both $A_\mathcal{E}(t, \tau)$ and $\phi_\mathcal{E}(t, \tau)$ determining the exact location of the range sidelobes in the frequency domain [10], [33], [57]. It is important to note that the range sidelobes caused by nonlinearities differ from *spectral sidelobes* resulting from the Gibbs phenomenon, in that they cannot be suppressed through the application of a window function [55]. For brevity, in the rest of this paper the term *sidelobes* will be used exclusively to refer to range sidelobes caused by amplitude and phase nonlinearities, with the term *spectral sidelobes* used to describe the sidelobes caused by the Gibbs phenomenon.

**TABLE 1.** A summary list of symbols and their corresponding parameters used in this paper.

| Symbol | Parameter |
|---|---|
| $A_{LO}$ | Amplitude of $S_{LO}$ |
| $A_{RF}$ | Amplitude of $S_{RF}$ |
| $A'_{LO}$ | Amplitude of $S'_{LO}$ |
| $A'_{RF}$ | Amplitude of $S'_{RF}$ |
| $A_\varepsilon$ | Amplitude nonlinearities of $S'_{LO}$ |
| $A_\xi$ | Amplitude nonlinearities of $S'_{RF}$ |
| $A_b$ | Amplitude of $S_b$ |
| $A'_b$ | Amplitude of $S'_b$ |
| $A_\mathcal{E}$ | Amplitude nonlinearities of $S'_b$ |
| $A_C$ | Amplitude constant terms of $S'_b$ |
| $B$ | Bandwidth |
| $S_b$ | Beat signal |
| $S'_b$ | Beat signal (containing nonlinearities) |
| $f_i$ | Instantaneous frequency |
| $f_0$ | Frequency at time $t=0$ |
| $f_1$ | Frequency at time $t=T_s$ |
| $f_b$ | Beat frequency |
| $\delta f$ | Frequency precision |
| $K$ | Frequency sweep rate |
| $\phi_{LO}$ | Phase of $S_{LO}$ |
| $\phi_{RF}$ | Phase of $S_{RF}$ |
| $\phi'_{LO}$ | Phase of $S'_{LO}$ |
| $\phi'_{RF}$ | Phase of $S'_{RF}$ |
| $\phi_\varepsilon$ | Phase nonlinearities of $S'_{LO}$ |
| $\phi_\xi$ | Phase nonlinearities of $S'_{RF}$ |
| $\phi_b$ | Phase of $S_b$ |
| $\phi'_b$ | Phase of $S'_b$ |
| $\phi_\mathcal{E}$ | Phase nonlinearities of $S'_b$ |
| $\varphi$ | Linear phase terms of $S'_b$ |
| $R$ | Range to the target |
| $\Delta R$ | Range bin spacing |
| $\delta R$ | Range resolution |
| $S_{LO}$ | Signal at LO mixer port |
| $S'_{LO}$ | Signal at LO mixer port (containing nonlinearities) |
| $S_{RF}$ | Signal at RF mixer port |
| $S'_{RF}$ | Signal at RF mixer port (containing nonlinearities) |
| $\alpha$ | Spectral window widening factor |
| $c$ | Speed of light |
| $T_s$ | Sweep duration |
| $t$ | Time |
| $\tau$ | Two-way travel time |

The SNR of FMCW radar systems is generally limited by the effects of the nonlinearities (i.e. sidelobes) close to the beat frequency, and by phase noise (Section II-E) far from the beat frequency [58], with amplitude and phase nonlinearities both distorting the shape of the pulse and increasing the sidelobe levels.

## K. NON-LINEARITY CORRECTION STRATEGIES
The beat signal, $S'_b(t, \tau)$, as described in Section II-I, can be thought of as resulting from the frequency domain representation of an ideal system (i.e. one with a constant sweep amplitude and perfectly linear phase ramp), as outlined in Section II-B, that has been *convolved* with the frequency domain representation of combined amplitude nonlinearities $A_\mathcal{E}(t, \tau)$ and phase nonlinearities $\phi_\mathcal{E}(t, \tau)$, as outlined in Section II-J. In essence, FMCW radar *deconvolution* seeks to characterize, and correct for, the deviation in amplitude from a constant value (across the sweep), and the deviation in phase from a perfectly linear phase ramp; and unlike pulse radar systems, the deconvolution of FMCW radar systems occurs in the time domain rather than the frequency domain.

There are two general strategies that are provided in the literature to correct for FMCW nonlinearities: hardware correction methods, and software correction methods, with both recently summarized by [30]. Hardware methods aim to correct the nonlinearities during signal generation, for example through the use of pre-distortion applied to the VCO used to generate a chirp signal [32], [59]. Software methods are different in that they are applied directly to the beat signal, in post-processing, which has the advantage of not requiring any additional hardware; two types of software correction methods commonly used: direct beat signal correction methods, and methods based upon a mathematical model of the beat signal [30].

Direct beat signal correction methods use the response from a reference target to first characterize the amplitude nonlinearities, $A_\mathcal{E}(t, \tau)$, and phase nonlinearities, $\phi_\mathcal{E}(t, \tau)$, and then apply a correction to the nonlinearities; with a variety of different techniques proposed in the literature [30], [42], [55], [58], [60]. The advantage of this approach is that it does not require any simplifying signal model assumptions, because the actual recorded nonlinearities are used to generate the correction. In Section II-I we saw that it is the two-way travel time, $\tau$ (or equivalently range, $R$), that determines exactly how the nonlinearities are incorporated into the beat signal (via (10)); however, direct beat signal correction methods assume that the nonlinearities are fixed (i.e. do not change with $\tau$); this makes the corrections very effective when applied to targets with ranges close to that of the reference target, but with correction effectiveness decaying with increasing range offsets [61], [62].

The other software correction methods are based upon mathematical models of the beat signal that use simplifications of the nonlinearities to allow their effective use over the whole range profile [30], [56], [63], [64], [65]. The effectiveness of this kind of approach is limited by the models used to simplify the nonlinearities. As mentioned in [30], and described in Section II-H, the nonlinearities in the beat signal can be divided into two parts: the nonlinearities in the transmitted signal and the nonlinearities in the received signal. Many of the signal model based approaches only consider the dominant transmitted nonlinearities of the frequency generator (i.e. the VCO) with the nonlinearities of other hardware devices in the system not included. To simplify the problem they assume that the receive nonlinearities are only time-delayed versions of the transmitted nonlinearities

i.e. $A_\xi(t, \tau) \approx A_\varepsilon(t - \tau)$ and $\phi_\xi(t, \tau) \approx \phi_\varepsilon(t - \tau)$. The received RF signal is thus modeled as a time-delayed version of the LO signal i.e. $S'_{RF}(t, \tau) \approx S'_{LO}(t - \tau)$ with the nonlinearities in the entire range profile compensated by making the nonlinearity corrections range independent, through the use of parametric models such as quartic polynomials [65], near range differential approximations [63], or using Residual Video Phase (RVP) methods [56], [64].

## III. DATA COLLECTION AND PROCESSING

In this section we give a brief overview of the KuKa radar hardware, and how data were acquired during the MOSAiC expedition. We also describe the KuKa calibration experiments that were performed during MOSAiC, and the use of newly-opened lead to obtain the radar impulse response.

### A. KUKA RADAR HARDWARE

The Ku- and Ka-band dual-frequency, fully-polarimetric radar (KuKa) was built by ProSensing Inc. specifically for operation in cold and polar environments, with full details of the system described in Stroeve et al., 2020 [26], hereafter referred to as *S2020*. In the rest of this section we provide a brief summary of the KuKa radar system and key radar system parameters.

The KuKa radar system is composed of two separate, and independent, radio frequency (RF) units, one for Ka-band and the other for Ku-band. Both units are dual-polarization, solid-state FMCW radar systems that use a linear FMCW modulation scheme using a fast linear FM synthesizer and pulse-to-pulse polarization switching. The Ka-band RF unit transmits signals over a frequency range of 30-40 GHz and the Ku-band RF unit transmits signals over a frequency range of 12-18 GHz; with both units utilizing very low power transmitters, suitable for operation at ranges of typically less than 30 m. The Ka-band and Ku-band RF units employ a two-antenna homodyne FMCW radar architecture, the antennas of each unit are dual-polarized scalar horns mounted on arms that extend away from the RF unit with a beamwidth of 11.9° for the Ka-band antenna (at 35 GHz) and 16.9° for the Ku-band antenna (at 13.575 GHz); and a polarization isolation between transmit and receive antennas of greater than 30 dB; no near-field correction is needed, since the antenna far-field distance is about 1 m.

The KuKa radar system transmits and receives in six instrument states: there are four radar channels containing transmit-receive polarization combinations: HH, VV, HV, VH (following the scattering matrix convention: the first letter indicates the receive polarization and the second letter the transmit polarization); with two additional channels also collected: a calibration loop signal (Cal) and a noise signal (Noise). Each chirp signal is transmitted over a duration of $T_s = 2$ ms, followed by a reset time of 200 $\mu$s. This results in a total chirp repetition interval of 2.2 ms. The total time required to acquire data from all six instrument

states ($6 \times 2.2$ ms $= 13.2$ ms), and to write the data to disk, is known as the group interval. For the Ka-band and Ku-band systems the group intervals are 0.33 s and 0.5 s, respectively.

The KuKa radar receiver uses a 14-bit Analog-to-Digital Converter (ADC) with a sample rate of 20 MHz; the range window of interest ($<30$ m) allows the sampling rate to be reduced (after low pass filtering and digitization) by a decimation factor of 16 for Ka-band and 32 for Ku-band, giving an effective sampling frequency of 1.25 MHz for Ka-band and 0.625 MHz for Ku-band; and a maximum unambiguous range of 17.7 m for Ka-band and 14.4 m for Ku-band.

Raw KuKa beat frequencies do not correspond to the phase center of the antennas, but instead correspond to the time delay between the transmitted signal that is routed into the LO port of the mixer, $S'_{LO}(t)$, and the received signal that is routed into the RF port of the mixer, $S'_{RF}(t, \tau)$ (Section II-A). A beat signal (Section II-C, II-I) with a frequency of 0 Hz thus corresponds to the range where the time delay in the LO path equals the time delay in the RF path (Fig. 1). A range correction factor known as the *range to antenna* is provided by the manufacturer for both the Ka-band and Ku-band RF units, 2.07 m for Ka band and 2.37 m for Ku-band, in order to correct the beat-signal-derived ranges to ranges that are relative to the antenna phase center. We summarize the key KuKa radar system parameters in Table. 2.

### B. KUKA DATA ACQUISITION

The separate KuKa Ka-band and Ku-Band RF units can be combined to operate in two different configurations: as a scatterometer (known as scan mode) or as an altimeter (known as stare mode).

In scan mode, the Ka-band and Ku-band RF units (plus antenna arms) are attached to an elevation-over-azimuth positioner system (mounted on a large sled) that allows KuKa to scan over a programmed range of azimuth and incidence angles (at specific increments), with an 85 cm lateral separation between the Ka-band and Ku-band antennas [26], [66], [67].

In stare mode, both Ka-band and Ku-band RF units (and antenna arms) are mounted to a ridged metallic frame that is attached to a smaller sled known as the *transect sled*, with a 70 cm lateral separation between the Ka-band and Ku-band antennas. In stare mode KuKa measures the backscatter at nadir (as a function of time) as the transect sled is towed across the snow surface [26], [27].

The Ka-band and Ku-band RF units produce separate binary files, corresponding to data collected over a user defined time interval (typically 5 minutes). The data within each binary file are organized into so-called *data blocks*, with each data block containing the data acquired in all six instrument signal states. The Ka-band system produces a new data block every 0.33 s and the Ku-band system produces a new data block every 0.5 s; however, data acquisition is

**TABLE 2.** Summary of the key KuKa radar system Ka- and Ku-band specifications, modified from [26].

| Radar parameter | Ka-band value | Ku-band value |
|---|---|---|
| Chirp frequency range | 30-40 GHz | 12-18 GHz |
| Chirp length | 2 ms | 2 ms |
| Group interval | 328 ms | 499 ms |
| Bandwidth | 10 GHz | 6 GHz |
| Range resolution (theoretical) | 1.5 cm | 2.5 cm |
| Range resolution (after Hann windowing) | 2.4 cm | 4.1 cm |
| Transmit power | 6 dBm | 10 dBm |
| Transmit-receive polarization | VV, HH, HV, VH | VV, HH, HV, VH |
| Antenna diameter | 0.09 m | 0.15 m |
| Antenna 6 dB beamwidth | 11.9° at 35 GHz | 16.9° at 13.575 GHz |
| Transmit-receive antenna spacing | 7.65 cm | 13.36 cm |
| Cross-polarization isolation | > 30 dB | > 30 dB |
| Analog-to-digital converter frequency | 20 MHz | 20 MHz |
| Decimation factor | 16 | 32 |
| Effective sampling frequency | 1.25 MHz | 0.625 MHz |
| Range-to-antenna correction factor | 2.07 m | 2.37 m |
| Maximum unambiguous range | 17.7 m | 14.4 m |
| Analog-to-digital converter resolution | 14 bit | 14 bit |

not precisely time-aligned between the Ka-band and Ku-band radar (start times can vary by ∼0.5 s).

The binary data can be read by the original ProSensing IDL software, a MATLAB® translation of the IDL software, or the recently developed Python-based package (KuKaPy). Data for each instrument state (HH, VV, HV, VH, Cal, Noise) are originally in a unit of counts, which is converted to voltage via multiplication with a constant. The voltage data are arranged into arrays, $\mathbf{D}$, containing the real-valued time-domain representation of the beat signal, $S_b'$ (described in Section II-I). There are separate voltage data arrays for each of the six instrument states (i.e. $\mathbf{D}_{VV}$, $\mathbf{D}_{HV}$, $\mathbf{D}_{VH}$, $\mathbf{D}_{HH}$, $\mathbf{D}_{Cal}$, $\mathbf{D}_{Noise}$), each having $X$ rows and $Y$ columns, arranged as follows,

$$\mathbf{D} = \begin{bmatrix} d_{11} & d_{12} & d_{13} & \dots & d_{1Y} \\ d_{21} & d_{22} & d_{23} & \dots & d_{2Y} \\ d_{31} & d_{32} & d_{33} & \dots & d_{3Y} \\ \vdots & \vdots & \vdots & \ddots & \vdots \\ d_{X1} & d_{X2} & d_{X3} & \dots & d_{XY} \end{bmatrix}$$

with the $y$'th column of each array associated with the same data block.

The beat signal voltage arrays, $\mathbf{D}$, can also be converted into two other forms: they can be converted into their analytic (complex) time-domain form, $\mathcal{H}\{\mathbf{D}\}$, through the application of a column-wise Hilbert transform [68]. The voltage arrays can also be converted into echograms containing the power spectral density of the received voltage, $\mathcal{F}\{\mathbf{D}\}$, through the application of a Hann spectral window followed by a column-wise Fast Fourier Transform (FFT).

The echogram representation of the voltage arrays, $\mathcal{F}\{\mathbf{D}\}$, follows the radar data cube convention [69], with rows

$x = 1, 2, 3, \dots, X$ representing *fast-time* samples corresponding to specific range bins (Section II-D), and columns $y = 1, 2, 3, \dots, Y$ representing *slow time* and corresponding to specific data blocks. The time-domain beat signal data, $\mathbf{D}$, can also be processed using KuKaPy (or equivalent) to produce echograms of calibrated polarimetric backscatter [26], [27], [66], [67].

### C. KUKA DEPLOYMENT AT MOSAIC

The KuKa radar system was deployed at MOSAiC (Multidisciplinary drifting Observatory for the Study of Arctic Climate), during Leg 1, Leg 2 and Leg 5 [25]. The main deployment of KuKa at MOSAiC was during Legs 1 and 2, with KuKa being deployed in both scan (scatterometer) and stare (altimeter) modes [26], [27], [66], [67].

In scan mode, KuKa was mounted on its pedestal riser and installed at the MOSAiC Remote Sensing (RS) site, with the physical location of the RS site moved twice during MOSAiC due to lead opening and deformation events. At the RS site KuKa was powered by the ship's power (240 V AC 50 Hz power) via the Uninterruptible Power Supply (UPS). Data collection involved near-hourly (55 min) scanning across 90° azimuth and incidence angles between 0° and 50° at 5° increments at RS site [26], [66], [67].

In stare mode, two 12 V DC batteries were used to power the KuKa RF units, data collection involved repeated weekly transects of 1-8 km in length; with supporting ancillary data also collected [26], [27]. The first deployment of KuKa was on the 18 October 2019 at the RS site, and KuKa was then deployed in both scan and stare modes until 31 January 2020, after which the radar was packed up for maintenance.

Stare mode transects were made over both the *Northern transect* and *Southern transect* loops, with the Northern

transect representing thicker and rougher ice and the Southern transect representing younger and thinner ice. During leg 1 data were collected over two short Northern transects, and one frost flower event (sampled over thin ice). The majority of the stare mode transects occurred during Leg 2: weekly transects started on the 20 of December 2019 and ran until the 30 January 2020. There were also two transects over First Year Ice (FYI) along the runway that was built on the port side of the RV Polarstern; as well as, two *Lead transects* spaced a day apart. In total there were 13 stare mode transects of KuKa during leg 1 and 2 (See S2020 [26] and [27] for more details).

### D. KUKA CALIBRATION DURING MOSAIC

To characterize the performance of a radar system, such as KuKa, requires knowledge of the radar impulse response (also known as the radar system response). One way to characterize the impulse response is through the use of a system *loopback* measurement using a delay line. The KuKa radar system contains an internal calibration loop that consists of an attenuator together with a 4.2 m long delay line. The KuKa RF units are insulated and heated to stabilise their internal temperatures in cold polar conditions, but the internal calibration loop allows the data processing software to track gain variations within the system, and to further compensate for any residual power drift, due to temperature changes, that occur during data collection [26].

As mentioned in S2020, the internal calibration loop does not track and compensate for the gain variations of RF components that are outside of the calibration loop, including the cables to the antenna and the antenna ports. The transfer function of the antennas themselves can also add additional complexity that needs to be quantified [23], [30]. To fully characterize the radar impulse response thus requires a calibration target that is *external* to the radar system, such as a corner reflector. A corner reflector calibration was performed at the RS site on 16 January 2020: a trihedral corner reflector was positioned at a range of 10 m and used to calculate the radar cross-section per unit area (NRCS) and polarimetric quantities. Unfortunately, these data were subsequently lost, and as a result, are not available for further analysis. The corner reflector calibration also had limitations, the 10 m range offset was far outside the stare mode operating range (Section II-K), and the radar return from a corner reflector can incorporate multiple off-nadir surface returns (at different ranges) from within the antenna beamwidth.

In S2020, an experiment was also performed to compare the impulse response obtained from the calibration loop with the impulse response obtained from a metal plate (that was placed on the snow surface). The metal plate experiment served as a vertical height reference for KuKa radar returns, with the measured range to the peak associated with the metal plate (of thickness 2 cm) being 1.53 m; when the metal plate was removed the air-snow peak appeared at about 1.55 m in both Ka- and Ku- band data. Although there was a fairly good qualitative agreement in the shape of the impulse response

between the metal plate and calibration loop data (at both Ka-band and Ku-band at VV polarization), there were also significant differences especially at greater ranges from the main lobe peak.

The metal plate experiment was useful to provide a vertical height reference, but was not optimal to obtain the impulse response. There was a lip running around the edge of the plate meaning that there would have been additional radar returns from the lip in addition to the flat central region, confounding waveform interpretation.

Another factor influencing the measurements was the size of the metal plate. To accurately characterize the impulse response, a flat and smooth metal sheet of sufficient dimensions is required to avoid issues with off-nadir returns. The sheet dimensions should accommodate the first Fresnel zone, beam-limited footprint and pulse-limited footprint [70], [71], [72]. The pulse-limited footprint refers to the area on the surface that is illuminated by a single radar pulse; its diameter, $F_{\text{Pulse}}$, is calculated using,

$$F_{\text{Pulse}} = 2 \cdot \sqrt{\frac{H c \alpha}{B}} \qquad (40)$$

where $H$ is the height of the antenna phase center above the surface, $c$ is the speed of light, $\alpha$ is the spectral window widening factor and $B$ is the bandwidth. The beam-limited footprint refers to the area on the surface illuminated by the antenna gain pattern. Its diameter, $F_{\text{Beam}}$, is calculated using,

$$F_{\text{Beam}} = 2H \cdot \tan\left(\frac{\beta}{2}\right) \qquad (41)$$

where $\beta$ represents the antenna beamwidth. The diameter of the first Fresnel zone (i.e. the Fresnel-limited footprint) is given by,

$$F_{\text{Fresnel}} = \sqrt{2 H \lambda_c} \qquad (42)$$

where, $\lambda_c$ is the wavelength at the center frequency.

Using the values in Table 2, equations (40), (41), (42), and $\alpha = 1.62$ (from Section II-D); we can calculate footprint diameters for a height value of $H = 1.55$ m (corresponding to the air-snow peak location). For Ka-band: $F_{\text{Pulse}} = 55$ cm, $F_{\text{Beam}} = 32$ cm and $F_{\text{Fresnel}} = 16$ cm. For Ku-band $F_{\text{Pulse}} = 71$ cm, $F_{\text{Beam}} = 46$ cm and $F_{\text{Fresnel}} = 26$ cm. From these calculations which we also see that the KuKa radar system is beam-limited, as $F_{\text{Beam}} < F_{\text{Pulse}}$.

The metal plate used at MOSAiC was approximately $15 \times 55$ cm in size, and as a result was not wide enough to completely cover the first Fresnel zone, and its width was far too small to accommodate the beam-limited footprint; any radar returns from the surface of the metal plate would have thus also included returns from the snow surface.

### E. THE KUKA LEAD TRANSECTS

Sea ice formed within newly opened leads has been used to characterize the radar impulse response in airborne FMCW radar datasets collected during sea ice survey missions [22],

[23]. Under calm conditions the new ice growing within a recently opened lead takes the form of smooth, highly-saline, elastic, sheets of ice up to 10 cm thick known as *Nilas* [73], [74]. Over time, the initially optically smooth (at radar wavelengths) nilas surface is roughened by the appearance of *Frost flowers*: which are clusters of dendritic ice crystals, typically a few centimeters in diameter that grow over a period of hours to days under specific atmospheric conditions of temperature, relative humidity and wind speed [75], [76]. The relatively smooth, and highly saline, nature of nilas can provide a natural alternative to a large metal sheet calibration target.

At MOSAiC a lead ∼50 m wide and ∼1 km long opened on the 21 January 2020. A photograph of lead surface conditions on the 23 January is shown in Fig. 2a from which we observe a lead surface comprised of nilas with a high percentage coverage of frost flowers. The frost flower coverage is non-homogeneous with regions of bare ice visible between denser regions of frost flowers. The dark shade of the nilas is indicative of high brine concentrations, an extracted ice sample had a measured bulk salinity of 17 ppt, and a measured ice thickness of 7.5 cm. Lead surface conditions on the 24 January is shown in Fig. 2b, the measured ice thickness (from an ice core) had increased to 10 cm, with the surface ice salinity (from the top 1 cm of an ice core) measured to be ∼36 ppt [26]

KuKa stare mode lead transects were performed on both the 23 and 24 of January, two on the 23 January and four on the 24 January. During each transect the sled (containing KuKa) was dragged along the undulating edge of the lead with both the Ka- and Ku-band antennas pointed toward the lead surface (as shown in Fig. 3). From Fig. 3, we see that when KuKa is positioned along the edge of the lead, a distance of 0.9 m separates the edge of the transect sled (i.e. the lead edge) and the antenna boresight.

The mean range to the nilas surface within the lead determined from KuKa measurements (see Section IV-A) is $H = 1.8$ m. Using the values in Table 2, and (41), (42), we can again calculate the footprint diameters. For Ka-band: $F_{Beam} = 38$ cm and $F_{Fresnel} = 18$ cm; whereas, for Ku-band $F_{Beam} = 53$ cm and $F_{Fresnel} = 28$ cm. The maximum KuKa Fresnel limited footprint is 28 cm and the maximum beam limited footprint is thus 53 cm. From Fig. 3, we see that this geometry thus allows for an unobstructed radar return from the nilas surface within the lead, from which the KuKa radar impulse response may be obtained. The radar return will also likely be non phase-coherent due to the roughening effect of frost flowers; with the exception being the small isolated bare ice regions between frost flower clusters.

It should be noted that a small area of open water and thin ice with frost flowers was also sampled on the 23 November 2019, however limited data were collected, and KuKa remained stationary during the entirety of data collection so these data are not used in the subsequent analysis.

## IV. METHODOLOGY

In this section, we outline the processing steps required to use the impulse response data collected during the KuKa lead transects to generate deconvolution waveforms that can be applied to the entire KuKa MOSAiC dataset to suppress the sidelobes and improve data quality.

### A. THE KUKA IMPULSE RESPONSE

In this section we analyze KuKa data collected during the lead transects (Section III-E) to characterize the KuKa radar impulse response. The voltage arrays, **D**, acquired during the lead transects were processed into echograms through the application of a Hann spectral window, followed by a column-wise FFT (Section III-B). Fig. 4 shows example echograms from data collected during a lead transect on 24 January 2020 (Section III-E); these data also correspond to the lead data that were shown in S2020 (their Fig. 10 [26]). In S2020 it was shown that the VV and HH signal power were very similar (their Fig. 8); thus for brevity in Fig. 4 (and the rest of this paper) we only show data for the Ka VV, Ka HV, Ku VV and Ku HV transmit-receive polarization combinations.

The dominant signal observed in Fig. 4 is the return from the surface of the nilas within the lead, which is seen to undulate between 1.5-2 m in all echograms. These undulations are due to changes in the relative range between the KuKa antennas and nilas surface as KuKa was dragged along the undulating lead edge. In Fig. 4 we also see signal *artifacts* that are present in all bands and polarizations. In general two types of artifacts are observed: *range-independent artifacts* that are independent of target range, and *range-dependant artifacts* are dependent on target range.

The range-independent artifacts are associated with the KuKa radar receiver and can occur even in the absence of a transmitted signal. The two classes of range-independent artifacts seen in Fig. 4 are the leakage signal (Section II-G) and faint in-band spurious signals (Section II-F). The leakage signal is represented in Ka VV and Ka HV echograms as horizontal bands extending from a range of −2 m to zero range (i.e. the range of the antenna phase center). In Ku VV and Ku HV echograms the leakage signal banding is seen to extend from −2 m to below the nilas surface return; the Ku-band leakage signal is also much more prominent (than the Ka-band) and tends to dominate the noise floor. Faint in-band spurious signals are seen in Ka VV and Ka HV echograms at a range of ∼6.5 m and between 9.0-9.5 m. These spurious signals could potentially be caused by intermodulation products (Section II-F), but they are both low in power and located away from the surface return, so have little effect on data quality.

The range-dependant artifacts tend to undulate in unison with the nilas surface return. The two classes of range-dependent artifacts are sidelobes (Section II-J) and radar multiples; with multiples due to either harmonics, unwanted reflections between the various radar system components
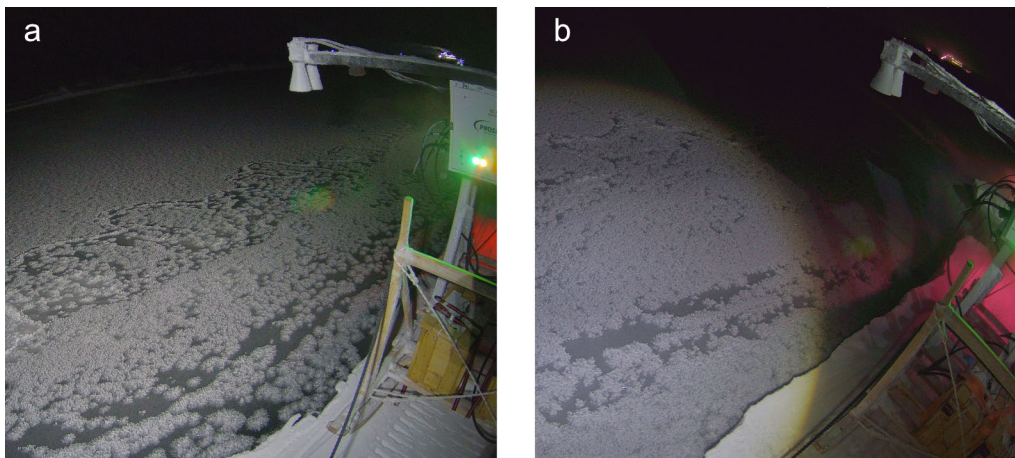
**FIGURE 2.** Photographs depicting lead surface conditions on (a) 23 January 2020 and (b) 24 January 2020. The KuKa radar system, featuring antenna arms and horns, is visible in the right half of each photograph.
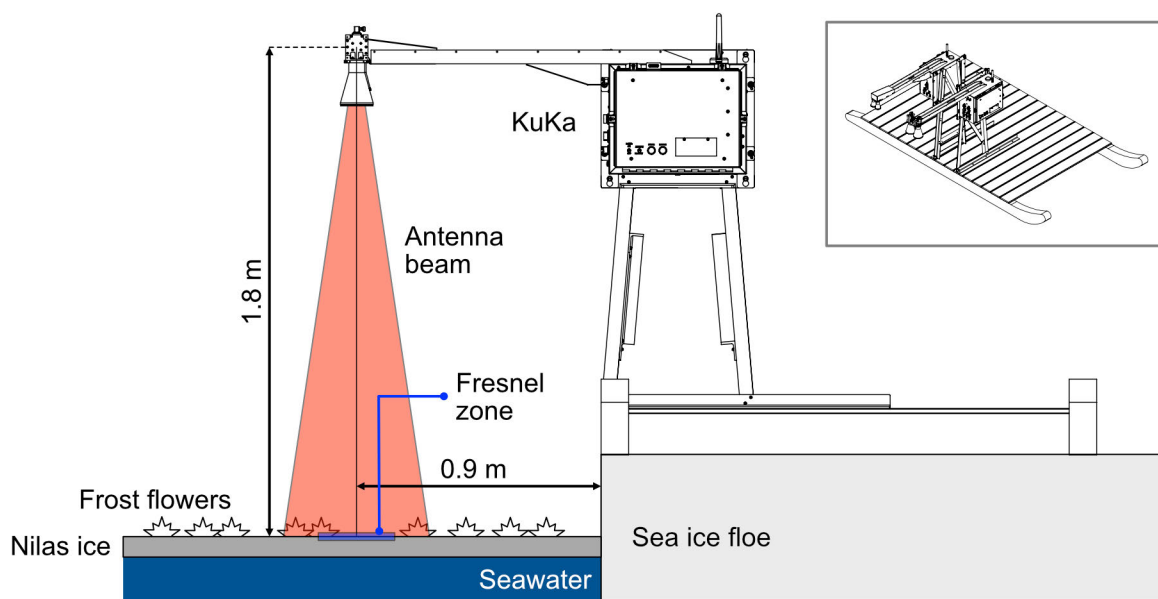


**FIGURE 3.** Diagram illustrating the KuKa radar system in stare mode configuration while conducting a transect along the lead edge. The inset provides a projected view of the KuKa system mounted on the transect sled (Modified from ProSensing Inc).

(Section II-F), or multiple reflections between the KuKa antennas and nilas surface. Sidelobes are represented in echograms as discrete bands that occur on either side of the undulating nilas surface return, and are generally seen between ranges of 1-3 m, appearing more prominent in the co-polarized echograms (Ka VV, Ku VV) than the cross-polarized echograms (Ka HV, Ku HV). It is also worth noting that the sidelobes for Ku HV appear almost completely obscured by the leakage signal.

Radar multiples are seen as fainter versions of the original nilas surface return, but occurring at greater ranges than the original return. In the Ka VV echogram we see distinct radar multiples at between 3-4 m and 9-10 m, and a much fainter multiple at between 5-6 m; whereas, for Ka HV we only observe a single distinct multiple at between 3-4 m. For Ku

VV we see a radar multiple at between 3-4 m and two fainter multiples at between 5.5-6.5 m and 9.5-10.5 m; for Ku HV a single multiple is observed at between 3-4 m, again partially obscured by the leakage signal. The radar multiples at 3-4 m and 5-6.5 m are most likely due to the multiple reflections between the KuKa antennas and nilas surface. The absence of a visible return at between 7-8 m indicates that the 9-10.5 m multiples are likely due to harmonics (or intermodulation products) rather than multiple reflections.

### B. REMOVING THE LEAKAGE SIGNAL
In Fig. 4, we saw that the leakage signal manifests itself as a zone of horizontal banding extending from −2 m to 0 m (for Ka-band data), or to ranges below the nilas surface return (for Ku-band data). In Fig. 5a we show the Ka VV echogram
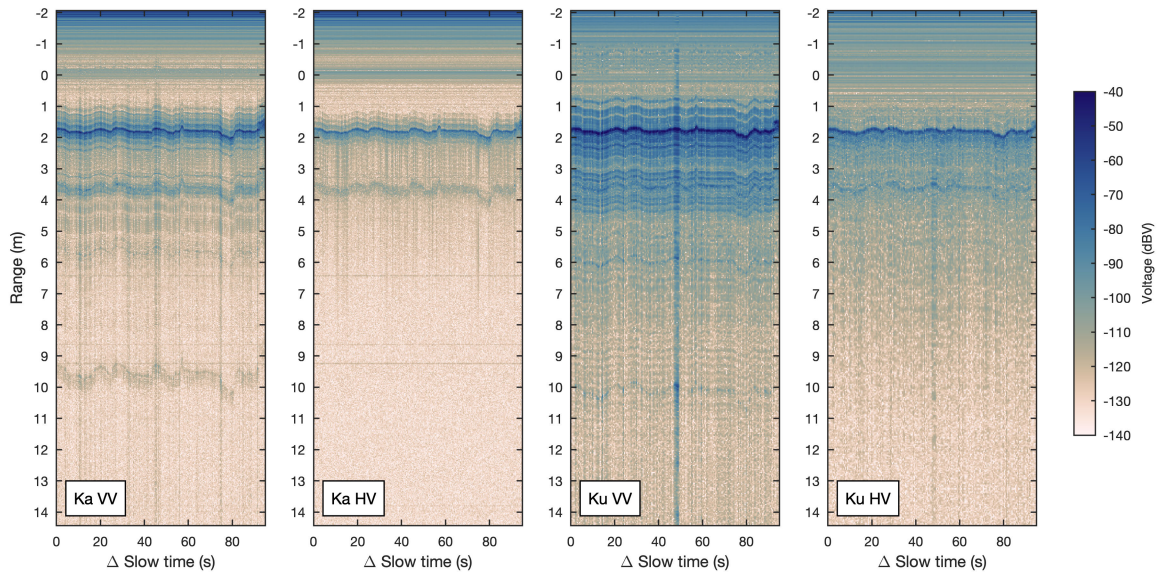
(from Fig. 4) over its entire maximum unambiguous range, and in Fig. 5c we show the corresponding real-valued beat signal in its original time-domain form (Section III-B). From Fig. 5c we see that the leakage signal is represented in the time-domain as a strong low frequency signal dominating the entire array; with higher frequency signals seen embedded within it. This effect is further highlighted in Fig. 6 where we have plotted, as a red line, the echogram column shown by the black dashed line (in Fig. 5c). As noted in Section II-I, the beat signal is actually formed from the linear superposition of returns from all $N$ individual targets, within the antenna FOV. Due to self-mixing (Section II-G), the leakage signal acts like a strong return with a beat frequency close to zero (i.e. DC); meaning that it too will be superimposed upon the other radar returns; causing it to dominate the time-domain signal (as shown in Fig. 6). Any radar returns from the surface will be embedded within the low frequency leakage signal; the application of nonlinearity correction techniques (Section II-K) would risk amplifying the leakage signal, introducing additional data artifacts in the process. The leakage signal must be removed before deconvolution can take place.

Leakage signal removal techniques have been applied to airborne FMCW radar data collected during cryosphere remote sensing campaigns [22], [23]. In the case of airborne data the leakage signal (also known as coherent noise) is seen to be independent of flight altitude and remain consistent over large along-track distances [19]. To characterize the leakage signal, slow time boxcar filters have been applied to the echograms, or the average calculated from a set number of contiguous echogram columns. These averaging operations

seek to isolate the leakage signal by reducing the relative power contributions from the fluctuating air-snow interface. Once characterized, the leakage signal is then subtracted from each column of the echogram potentially allowing the leakage signal to be completely removed without leaving any artifacts [19], [22], [23].

Leakage signal removal techniques, based upon slow time mean subtraction, become ineffective if the relative distance between the aircraft and the snow surface stays constant [22], [23]. Unfortunately, for the case of the KuKa radar system the range to surface is far more constant than the large vertical fluctuations seen in airborne data [26], so slow time leakage removal techniques are less effective. If a slow time mean is taken of these data, and removed, the average of the high frequency surface signals are also removed resulting in unwanted horizontal smearing of interfaces in the resultant echograms.

Due to the constraints imposed by a surface-based system (such as KuKa) we instead utilize a high-pass filter to remove the leakage signal. We first use (13) (and the range to antenna correction factor) to calculate the beat frequency associated with zero range (i.e. the phase center of the antenna). We design a Kaiser-window-based highpass finite impulse response (FIR) filter [43], [44] with a passband frequency equal to the zero-range beat frequency and a stopband attenuation of 100 dB. The high-pass filter is then applied to each column of **D**, i.e. the KuKa voltage arrays.

We revisit Fig. 5 to show the effect of the high-pass filter on the time-domain voltage data. In Fig. 5d, we see that the filtering operation effectively removes the low frequency banding that was observed in Fig. 5c. The effect of the
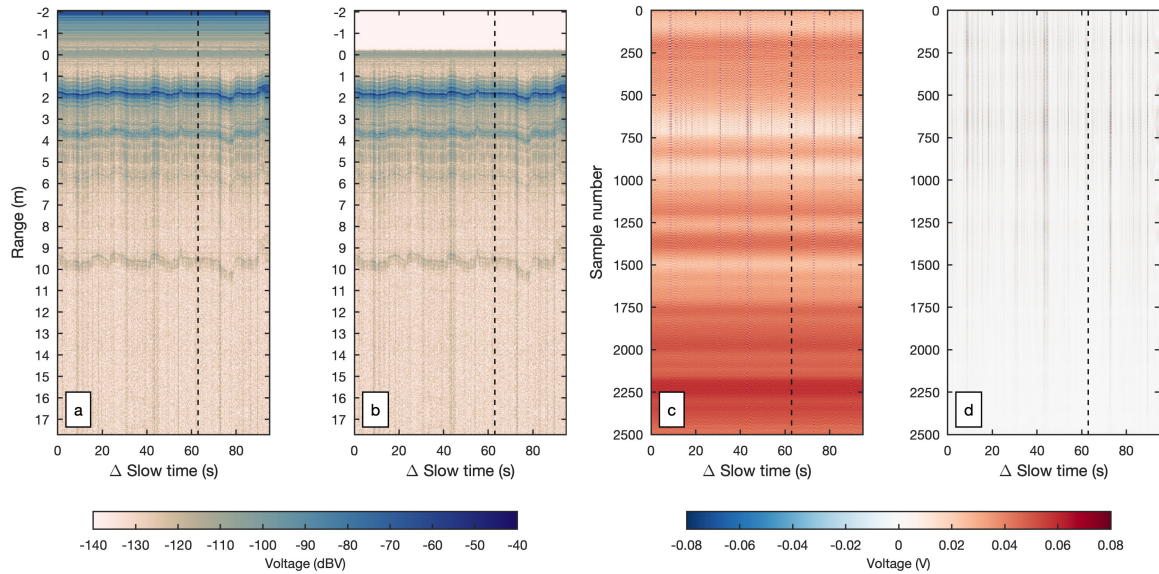
**FIGURE 5.** (a) Shows the Ka VV echogram (as depicted in Fig. 4) over its entire maximum unambiguous range. (b) Demonstrates the effect, on the Ka VV echogram, of high-pass filtering for leakage signal removal. (c) Exhibits the real-valued beat signal (as shown in (a)), but in its original time-domain form. (d) Presents the real-valued beat signal after high-pass filtering for leakage signal removal. The black dashed line indicates the location of data from which Fig. 6 is generated.
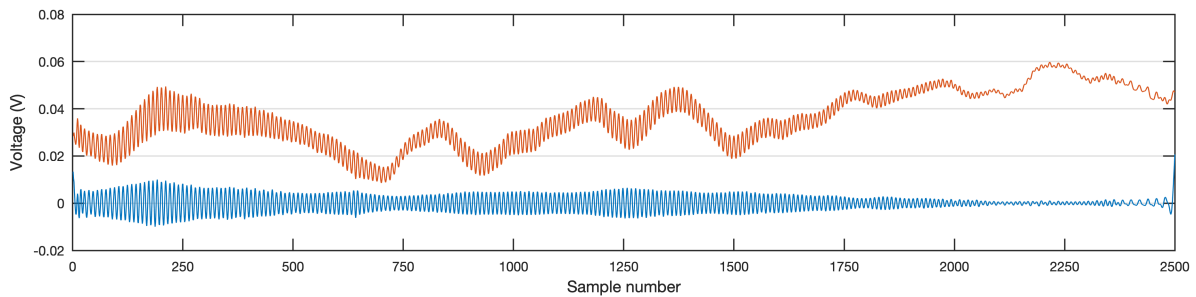


**FIGURE 6.** The voltage signal before and after leakage signal removal. The red line represents the signal before leakage signal removal and corresponds to the column indicated by the black dashed line in Fig. 5c. The blue line represents the signal after leakage signal removal and corresponds to the column indicated by the black dashed line in Fig. 5d.

filtering in the corresponding (frequency-domain) echogram is shown in Fig. 5b; here, we observe that signals at ranges less than 0 m are filtered out. Revisiting Fig. 6, the effect of the high pass filtering on the data is shown by the blue line, from which we can observe that the low-frequency signal component has been effectively removed. We can now also observe the effect of the amplitude modulation described in Section II-J. Although the high-pass filter effectively mitigates the leakage signal, there may still be some residual leakage-signal-derived in-band spurious signals at ranges greater than zero that cannot be removed, this is an unavoidable consequence of the near-constant range-to-surface of surface-based instruments such as KuKa.

### C. ISOLATING THE NILAS SURFACE RETURNS

As mentioned in Section II-J, the presence of amplitude nonlinearities, $A_{\mathcal{E}}(t, \tau)$, and phase nonlinearities, $\phi_{\mathcal{E}}(t, \tau)$, results in the amplitude and phase modulation of the beat signal, respectively. The modulating effects of the nonlinearities

increases the beat spectral bandwidth of the target response by spreading target energy into different frequencies, and away from the target's beat frequency. In echograms, nonlinearities manifest themselves as the discrete sidelobes that occur on either side of the dominant beat signal peak (i.e. the nilas surface return shown in Fig. 4) with the specific frequency content of both $A_{\mathcal{E}}(t, \tau)$ and $\phi_{\mathcal{E}}(t, \tau)$ determining the exact location of the sidelobes. The observed strength and range extent of the sidelobes (relative to the nilas surface return) can therefore be used to characterize the frequency content of the sidelobes, and thus the frequency content of the nonlinearities.

To accurately characterize the nonlinearities we must first isolate the sidelobes from the other signal artifacts (Section IV-A), as these artifacts will have their own amplitude and frequency content. To perform this isolation we will make use of a bandpass filter, with a passband designed to coincide with the frequency content of the sidelobes. We design a Kaiser-window-based bandpass FIR

filter with a sampling frequency set to the effective sampling frequency (Section III-A) and a stopband attenuation of 100 dB. From Fig. 4 we observe that the range to the nilas surface along a KuKa lead transect is not constant, due to the undulating lead edge (Section III-E), so the passband frequency range must vary depending upon the range to the nilas surface. To achieve this, copies of time-domain voltage arrays, **D**, for each band and polarization are zero padded (Section II-D), so that the number of rows is 100 times their original length (i.e 100 × 2500 for Ka-band and 100 × 1250 for Ku-band). The FFT of each column is then taken with the range to the nilas surface found by extracting the range of the maximum magnitude peak. From Fig. 4, we observed that harmonics (or radar multiples) occur at integer multiples of the nilas surface range. We can therefore define a bandpass range window where the range-to-nilas-surface in each column is multiplied by 0.5 to give the minimum window range, and multiplied by 1.5 to give the maximum window range. The edges of the bandpass range window are then converted to their corresponding beat frequencies (via (13)), again taking into account the range to antenna correction factor; giving the correct frequency range for the bandpass filter.

### D. ALIGNING THE NILAS SURFACE RETURNS

Any single radar return from the nilas surface will be affected by noise (Section II-E), residual leakage signal (Section II-G, IV-B), as-well as surface irregularities such as frost flowers (Section III-E). To accurately characterize the amplitude nonlinearities, $A_{\mathcal{E}}(t, \tau)$, and phase nonlinearities, $\phi_{\mathcal{E}}(t, \tau)$, requires the averaging of many nilas surface radar returns.

Revisiting Fig. 2 and 3, we can make the simplifying assumption that the radar returns from the nilas surface will be dominated by returns from within the first Fresnel zone. In this case, the radar returns from the nilas surface can be modeled as single point target located at nadir. The beat signal arising from the lead surface return can then be expressed, via (31, 36, 37 and 39), as,

$$S_b'(t, \tau) = [A_C(t, \tau) \cdot A_{\mathcal{E}}(t, \tau)] \\ \cdot \exp\{i\,[\varphi(t, \tau) + \phi_{\mathcal{E}}(t, \tau)]\} \quad (43)$$

From Section II-K, the non-linear terms $A_{\mathcal{E}}(t, \tau)$ and $\phi_{\mathcal{E}}(t, \tau)$ can be assumed to be only weakly dependent on two-way travel time, $\tau$ (i.e. the range); however, the value of $\varphi(t, \tau)$ will be strongly dependent on $\tau$, and this dependence needs to be corrected for before any signal averaging can occur.

To correct for the $\tau$ dependence in (43) requires the application of a phase shift. From (32), the value of $\varphi(t, \tau)$, is given by,

$$\varphi(t, \tau) = \left[2\pi\left(f_0\tau - \frac{1}{2}K\tau^2\right)\right] + 2\pi\,(Kt\tau) \quad (44)$$

The terms within the square brackets represent a constant, so it is the value of the $2\pi\,(Kt\tau)$ term that determines the gradient of the phase ramp (i.e. the beat signal frequency).

To remove the $\tau$ dependence in (43) we must correct all the nilas surface returns to a single reference range.

The exact choice of reference range does not affect the final result (as long as the same value is used for all returns). Based upon the approximate range of the KuKa air-snow interface (surface return) peak over a level snow surface, we choose the reference range, $R_{ref}$, to be 1.5 m; with a corresponding reference two-way travel time, $\tau_{ref}$, given by,

$$\tau_{ref} = \frac{2R_{ref}}{c} \quad (45)$$

To correct for $\tau$ dependence in (43) we must apply a phase shift based upon the difference, $\tau - \tau_{ref}$. The phase shift requires that we use the analytic (complex) form of beat signal voltage arrays (Section III-B), obtained through the use of a column-wise Hilbert transform, applied to **D**, given as,

$$S_b'(t, \tau) = \mathcal{H}\{\mathbf{D}\} \quad (46)$$

with a phase shift applied to each column of $S_b'(t, \tau)$ to obtain,

$$S_{b,ref}'(t, \tau) = S_b'(t, \tau) \cdot \exp\left\{-i\,2\pi\left[Kt\left(\tau - \tau_{ref}\right)\right]\right\} \quad (47)$$

where here, $\tau$ is the two-way travel time associated with the range to the nilas surface (that was calculated in Section IV-C). The phase shift ensures that the phase ramp associated with each nilas surface return has the same gradient; in the echograms the phase shift also has the effect of aligning all the nilas surface returns peaks to the reference range ($R_{ref} = 1.5$ m).

### E. AGGREGATING THE LEAD RETURNS

To characterize the amplitude nonlinearities, $A_{\mathcal{E}}(t, \tau)$, and phase nonlinearities, $\phi_{\mathcal{E}}(t, \tau)$, voltage echograms (Section III-B) were made for all Ka- and Ku-band files collected during the KuKa lead transects of the 23 and 24 January 2020. In each of the echograms, radar returns from the surface of nilas (within the lead) are identified as contiguous *lead regions* with the following properties: high return power, prominent sidelobes, and having ranges greater than the reference range ($R_{ref} = 1.5$ m).

A list of *lead files* were compiled that contained nilas surface radar returns, and for each lead file the column numbers associated with each discrete lead region are saved. Some of the lead files contained only one lead region while others containing multiple lead regions, depending on the timing of the KuKa lead transects (Section III-E).

For the 23 January Ka-band lead files there were 437 *lead columns* with a mean range to nilas surface of 1.77 m ± 0.041 m, and for the Ku-band lead files there were a total of 292 lead columns with a mean range to nilas surface of 1.78 m ± 0.037 m. For the 24 January Ka-band lead files there were 1604 lead columns with a mean range to nilas surface of 1.83 m ± 0.089 m, and for the Ku-band lead files there were a total of 1034 lead columns with a mean range to nilas surface of 1.83 m ± 0.085 m.

The voltage arrays, **D**, containing the real-valued time-domain representation of the beat signal, are then aggregated

into separate arrays for each date (23, 24 January), band (Ka, Ku), and polarization (VV, HV, VH, HH) using the lead column numbers. Within each aggregated lead data array the leakage signal is first removed from each column using the high-pass filter method outlined in Section IV-B. The lead surface return for each column is then isolated using a bandpass filter (Section IV-C). In the last step all columns are aligned to the same reference range using the techniques described in Section IV-D. These steps produce arrays consisting of complex voltage which we term the *complex aggregated arrays*.

The processing steps for each date (23, 24 January), band (Ka, Ku), and polarization (VV, HV, VH, HH) can be summarized below as:

1) Use the lead column numbers to aggregate the real-valued time-domain voltage arrays, **D**, into an aggregated lead data array
2) Remove the leakage signal from each column of the lead data array using the highpass filter (Section IV-B)
3) Then isolate the nilas surface return in each column using the bandpass filter (Section IV-C)
4) Finally align the nilas surface returns in each column to the same reference range (Section IV-D)

### F. CHARACTERIZING THE AMPLITUDE NONLINEARITIES

The amplitude of the beat signal (containing nonlinearities), $S_b'(t, \tau)$, was in defined in Section II-J, via (35), as,

$$A_b'(t, \tau) = A_C(t, \tau) \cdot A_{\mathcal{E}}(t, \tau)$$

where, $A_C(t, \tau)$ is the constant amplitude term (36), which remains the same over sweep duration, $T_s$, and $A_{\mathcal{E}}(t, \tau)$ is the nonlinear amplitude term (37), which varies over $T_s$.

For the case of the complex aggregated arrays (Section IV-E), the column-to-column variability in $A_b'(t, \tau)$ is driven primarily by return power variability; due to the differing nilas surface conditions (i.e. frost flower coverage and associated surface roughness) within each KuKa footprint (Section III-E). To obtain an accurate estimation of $A_{\mathcal{E}}(t, \tau)$ we must average over multiple columns of the complex aggregated arrays; however, Root Mean Square (RMS) normalization must first be performed to remove the $A_C(t, \tau)$ dependence in (35).

To obtain $A_{\mathcal{E}}(t, \tau)$, the first step is to load the complex aggregated array associated with the required date (23, 24 January), band (Ka, Ku), and polarization (VV, HV, VH, HH). In the next step each column of the complex aggregated array is normalized, by dividing by its RMS, to form the complex normalized array. The magnitude of each element in the complex normalized array is calculated to create an array of normalized magnitudes. The mean is calculated across all columns of this normalized magnitude array to obtain a 1D array of mean magnitudes. In the final step the 1D mean magnitude array is itself normalized, by divided by its RMS, to obtain $A_{\mathcal{E}}(t, \tau)$.

Amplitude nonlinearities, $A_{\mathcal{E}}(t, \tau)$, are calculated for each date (23, 24 January), band (Ka, Ku), and polarization

(VV, HV, VH, HH), with the processing steps described above summarized here:

1) Load the required complex aggregated array (i.e. 23 January, Ka HV)
2) Divide each column of the complex aggregated array by its RMS value to form the complex normalized array
3) Calculate the magnitude of each element in the complex normalized array to form the normalized magnitude array
4) Take the mean across all columns of the normalized magnitude array to obtain the 1D mean magnitude array
5) Divide the 1D mean magnitude array by its RMS to obtain $A_{\mathcal{E}}(t, \tau)$

### G. CHARACTERIZING THE PHASE NONLINEARITIES

The phase of the beat signal (containing nonlinearities), $S_b'(t, \tau)$, was defined in Section II-J, via (38), as,

$$\phi_b'(t, \tau) = \varphi(t, \tau) + \phi_{\mathcal{E}}(t, \tau)$$

here, the nonlinear phase term $\phi_{\mathcal{E}}(t, \tau)$ is added to the linear phase ramp (i.e. the beat frequency), given by the $\varphi(t, \tau)$ term.

For the case of the complex aggregated arrays (Section IV-E), the column-to-column variability in $\phi_b'(t, \tau)$ is driven primarily by the phase contributions from the different nilas surface elements (such as frost flowers) within a KuKa footprint (Section III-E). To obtain an accurate estimation of $\phi_{\mathcal{E}}(t, \tau)$ we must again average over multiple columns of the complex aggregated array. This column averaging is made possible due to the phase multiplication in Section IV-D, that resulted in the phase ramp of each nilas surface radar return having the same gradient (i.e. $K\tau_{ref}$), with the phase ramp from a target at the reference range, via (44), given by,

$$\varphi_{ref}(t, \tau_{ref}) = 2\pi \left(Kt\tau_{ref}\right) \tag{48}$$

To obtain $\phi_{\mathcal{E}}(t, \tau)$ the first step is to load the complex aggregated array associated with the required date (23, 24 January), band (Ka, Ku), and polarization (VV, HV, VH, HH). The phase angle is then calculated for each element of the complex aggregated array to produce an array of phase angles. For each column of the phase angle array, the phase angles are unwrapped (by adding multiples $\pm 2\pi$ between consecutive phase angle values until the phase jump is less than $\pi$) to produce the phase ramp array. The mean is then calculated across all columns of the phase ramp array to obtain a 1D array containing the mean phase ramp. In the next step we subtract the reference phase ramp (48) from the 1D mean phase ramp array to obtain a 1D array of deramped phase angles. We then calculate the median of the 1D deramped array, and in the final step we take this median away from all elements of the 1D deramped array to obtain $\phi_{\mathcal{E}}(t, \tau)$.

Phase nonlinearities, $\phi_{\mathcal{E}}(t, \tau)$, are also calculated for each date (23, 24 January), band (Ka, Ku), and polarization (VV, HV, VH, HH), with the processing steps described above summarized here:

1) Load the required complex aggregated array (i.e. 24 January, Ku VV)
2) Calculate the phase angle for each element in the complex aggregated array to produce the phase angle array
3) Perform phase unwrapping for each column of the phase angle array to generate the phase ramp array
4) Take the mean across all columns of the phase ramp array to produce the 1D mean phase ramp array
5) Minus the reference phase ramp from the 1D mean phase ramp array to obtain the 1D deramped array
6) Calculate the median of the 1D deramped array, and then minus this median from the 1D deramped array to obtain $\phi_{\mathcal{E}}(t, \tau)$

### H. APPLYING DECONVOLUTION WAVEFORMS TO KUKA DATA

Examples of the amplitude nonlinearities, $A_{\mathcal{E}}(t, \tau)$, and phase nonlinearities, $\phi_{\mathcal{E}}(t, \tau)$, calculated from the 23 and 24 January lead transects are shown in Fig. 7; with the top panels in Fig. 7 showing $A_{\mathcal{E}}(t, \tau)$, and the bottom panels showing $\phi_{\mathcal{E}}(t, \tau)$. From Fig. 7, we see that the 23 January lead transect data (shown by the blue line) are very similar to the 24 January lead transect data (shown by the green line); with the small difference between the two transect days shown by the purple lines.

The lead transects on the 23 and 24 January were collected independent of each other, with nilas surface conditions (i.e. ice thickness and frost flower coverage) changing in the day between the transects (Section III-E). The observed similarities shown in Fig. 7 gives us confidence that the techniques outlined in Sections IV-B to IV-G are allowing the robust extraction of $A_{\mathcal{E}}(t, \tau)$ and $\phi_{\mathcal{E}}(t, \tau)$.

The amplitude nonlinearities, $A_{\mathcal{E}}(t, \tau)$, and phase nonlinearities, $\phi_{\mathcal{E}}(t, \tau)$, can be used to produce deconvolution waveforms. Revisiting (43), given as,

$$S_b'(t, \tau) = [A_C(t, \tau) \cdot A_{\mathcal{E}}(t, \tau)] \\ \cdot \exp\{i\,[\varphi(t, \tau) + \phi_{\mathcal{E}}(t, \tau)]\}$$

we can see that $A_{\mathcal{E}}(t, \tau)$ and $\phi_{\mathcal{E}}(t, \tau)$ can be combined to produce deconvolution waveforms, of the form,

$$\mathcal{W}_{\mathcal{D}}(t, \tau) = \frac{\exp\{-i\,\phi_{\mathcal{E}}(t, \tau)\}}{A_{\mathcal{E}}(t, \tau)} \tag{49}$$

which can be multiplied with $S_b'(t, \tau)$, to give,

$$\begin{aligned} S_{\mathcal{D}}(t, \tau) &= S_b'(t, \tau) \cdot \mathcal{W}_{\mathcal{D}}(t, \tau) \\ &= A_C(t, \tau) \cdot \exp\{i\,[\varphi(t, \tau)]\} \end{aligned} \tag{50}$$

From (50), we see that the application of the deconvolution waveform, $\mathcal{W}_{\mathcal{D}}(t, \tau)$, removes the nonlinear components of $S_b'(t, \tau)$, but will preserve the constant amplitude component $A_C(t, \tau)$, and the phase component associated with the range-to-target that is contained within $\exp\{i\,[\varphi(t, \tau)]\}$.

Separate deconvolution waveforms are produced for each date (23, 24 January), band (Ka, Ku), and polarization

(VV, HV, VH, HH). The deconvolution waveforms for the 23 and 24 January are then averaged to produce a composite set of deconvolution waveforms for each band (Ka, Ku) and polarization (VV, HV, VH, HH), that can be applied to the entire KuKa dataset.

The KuKa voltage data (Section III-B) for the Ka-band and Ku-band files are arranged into separate arrays for each polarization (i.e. $\mathbf{D}_{VV}, \mathbf{D}_{HV}, \mathbf{D}_{VH}, \mathbf{D}_{HH}$). To apply $\mathcal{W}_{\mathcal{D}}(t, \tau)$ to $S_b'(t, \tau)$ the leakage signal must first be removed from $\mathbf{D}$ using the high pass filtering techniques described in Section IV-B. The high-pass filtered voltage arrays are then converted to their analytic (complex) form, $\mathcal{H}\{\mathbf{D}\}$, through the application of a column-wise Hilbert transform [68]. Each column of the high-pass-filtered complex voltage arrays is then multiplied by the required deconvolution waveform (i.e. Ku VV, Ka HV) to produce the complex deconvolved array. In the final step, the real part of the complex deconvolved array is extracted to produce the deconvolved voltage array.

For each KuKa file (Ka-band or Ku-band), deconvolution waveforms are applied to each polarization (VV, HV, VH, HH), with the processing steps described above summarized here:

1) Load the required voltage array, e.g. $\mathbf{D}_{VV}$
2) Remove the leakage signal from each column of the voltage array using the highpass filtering techniques described in Section IV-B
3) Apply the Hilbert transform to each column of the high-pass-filtered voltage array
4) Multiply each column of the high-pass-filtered complex voltage array by the correct deconvolution waveform, $\mathcal{W}_{\mathcal{D}}(t, \tau)$, to produce the complex deconvolved array
5) Extract the real part of each element of the complex deconvolved array to obtain the deconvolved array, $S_{\mathcal{D}}(t, \tau)$

The software provided by ProSensing, or KuKa.py, can then be used to convert the deconvolved Ka- and Ku-band voltage data into echograms of calibrated polarimetric backscatter (Section III-B).

## V. RESULTS

In this section, we assess deconvolution effectiveness by analyzing KuKa data from three different survey dates: the lead transect dataset on January 24, 2020; the Northern transect dataset on January 16, 2020; and the Northern transect dataset on November 14, 2019. We use an echogram from each survey date to provide a qualitative description of deconvolution effectiveness, and a waveform from each echogram to provide a quantitative description of deconvolution effectiveness.

### A. ASSESSING DECONVOLUTION EFFECTIVENESS

Ideally, we would assess the effectiveness of the deconvolution waveforms, $\mathcal{W}_{\mathcal{D}}(t, \tau)$, described in Section IV-H, using a set of corner reflector and/or metal plate calibration experiments collected at regular temporal intervals during the
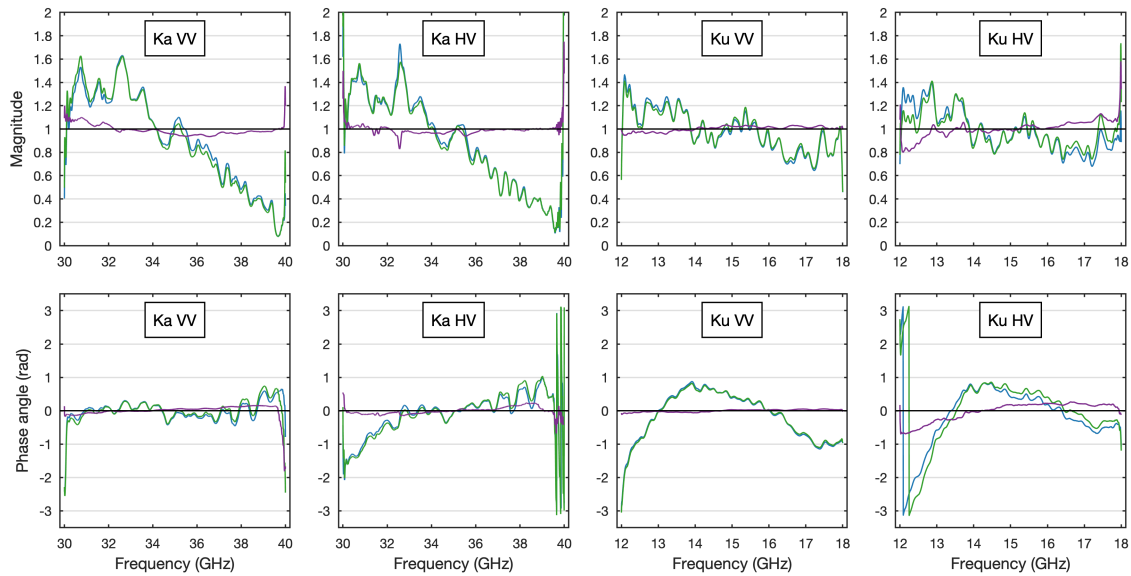
**FIGURE 7.** The KuKa nonlinearities. The top panels display the amplitude nonlinearities, $A_\mathcal{E}(t, \tau)$, while the bottom panels show the phase nonlinearities, $\phi_\mathcal{E}(t, \tau)$. The blue lines represent the 23 January lead transect data, the green lines represent the 24 January lead transect data, and the purple lines depict the difference between the two transect days.

campaign. Unfortunately, regular corner reflector/metal plate calibration experiments were not performed at MOSAiC, so such data are unavailable. Instead, we analyze Ka-band data (VV, HV) and Ku-band data (VV, HV) from three discrete stare mode survey dates (see S2020 [26] for details of KuKa deployment at MOSAiC).

The lead transect data from the 24 January 2020, will act as our reference dataset with a time offset of 0 days from when the deconvolution waveform data were collected (Section IV-H). The Northern transect data from the 16 January 2020, will act as our short time offset dataset with a time offset of 8 days from when the deconvolution waveform data were collected; survey data from this day were also discussed in detail in S2020 and [27]. The Northern transect data from the 14 November 2019, will act as our long time offset dataset with a time offset of 71 days from when the deconvolution waveform data were collected.

KuKa voltage data, $\mathbf{D}$, from each of the transect dates were deconvolved (Section IV-H), and echograms of calibrated polarimetric backscatter were produced (Section III-B). For each of the transect dates, we first provide a qualitative description of the effect of deconvolution on an example echogram from that date, describing the effect of deconvolution on the sidelobes and surface return clarity. We will then provide a quantitative description of deconvolution effectiveness by analyzing a typical waveform extracted from each of the example echograms.

In Section II-J, it was noted that the SNR of FMCW radar systems is generally limited by the effects of nonlinearities (i.e., sidelobes) close to the beat frequency and phase noise far from the beat frequency [58]; with both amplitude and phase nonlinearities distorting the shape of the pulse and increasing the sidelobe levels. If deconvolution completely corrects for

these nonlinearities, the radar return from a point target will closely resemble the applied spectral window (i.e. the Hann spectral window) until it encounters the noise floor or other spurious signals, such as the leakage signal.

Here we describe the five metrics that will be used to quantify the waveform properties before and after deconvolution:

- *Surface Return Peak (SRP)*
  This is the peak of the radar return associated with the first radar interaction with the (nilas or snow) surface.
- *Maximum Spurious Signal (MSS)*
  This is the maximum spurious signal that occurs at shorter ranges than the surface return peak, SRP, and that is independent of the surface return leading edge. For the case of optimal range sidelobe suppression the MSS will correspond to noise or to an in-band spurious signal (such as the leakage signal).
- *Spurious Free Dynamic Range (SFDR)*
  This is the power difference between the surface return peak, SRP, and the maximum spurious signal, MSS. Due to potential changes in the exact position of residual sidelobes (after deconvolution) the SFDR represents a relatively robust measure of deconvolution effectiveness.
- *Window Departure Point (WDP)*
  This is the point on the leading edge of the surface return where the power difference between the waveform and a colocated Hann spectral window is greater than $\sim$ 3dB.
- *Leading Edge Width (LEW)*
  This is the range difference between the surface return peak, SRP, and the window departure point, WDP. In essence, the LEW quantifies the surface return clarity (i.e. the leading edge of the surface return), with larger LEW values indicating a less ambiguous surface return.

We will also utilize the concept of relative change to quantify the change in the leading edge width, LEW, and the spurious free dynamic range, SFDR, after deconvolution. Here we define relative change as,

$$\text{Relative change} = \left( \frac{x - x_{\text{reference}}}{x_{\text{reference}}} \right) \times 100 \quad (51)$$

where $x_{\text{reference}}$ are the values before deconvolution.

### B. ZERO TIME OFFSET (LEAD TRANSECT)
This example is from the 24 January 2020, and represents a zero-time offset from when the nonlinearities were characterized. The results presented in this section demonstrate the effectiveness of the deconvolution waveforms for a specular impulse response dataset: the KuKa lead transects (section III-E).

#### 1) ECHOGRAM RESULTS
Echograms showing a subset of lead transect data from the 24 January 2020 are shown in Fig. 8, this is the same lead transect data that is shown in S2020 (their figure 10 [26]).

The upper set of panels in Fig. 8 displays KuKa echograms before deconvolution. In all bands and polarizations, a strong, specular radar return originating from the nilas surface is observed. Prominent and discrete sidelobes can be seen for Ka VV, Ka HV, and Ku VV. However, the sidelobes for Ku HV appear to be obscured by the leakage signal.

In the lower set of panels of Fig. 8, we observe the data after the application of deconvolution waveforms. It is evident that the sidelobes have been effectively suppressed for Ka VV, Ka HV, and Ku VV. However, only a marginal improvement is observed for Ku HV due to the presence of the leakage signal.

In the deconvolved data for all bands and polarizations, faint near-surface features that were not visible in the original data have become apparent. For instance, there is a noticeable feature at a slow time of approximately 40 seconds and at a range of 1.5 meters. Additionally, a faint diffuse return can be observed at greater ranges than the nilas surface return for all bands and polarizations.

The black dashed line in Fig. 8 indicates the location of the waveforms shown in Fig. 9. We will describe the waveform results in the following sections, and these results are also summarized in Table. 3.

#### 2) WAVEFORM RESULTS: KA VV
Before deconvolution, the SRP (Surface Return Peak) is located at a range of 1.79 m, with a power of −36 dB. The MSS (Maximum Spurious Signal) is located at 1.59 m, with a power of −60 dB; resulting in a SFDR (Spurious Free Dynamic Range) of 24 dBc. The WDP (Window Departure Point) is located at 1.74 m, resulting in a LEW (Leading Edge Width) of 0.05 m.

After deconvolution, the SRP remains located at 1.79 m, with a power of −34 dB. The MSS shifts to 1.67 m, with a power of −86 dB; resulting in an increased SFDR of 52 dBc. The WDP is located at 1.68 m, giving an expanded LEW

of 0.11 m. Deconvolution causes the SFDR to increase by 28 dB (a relative change of 117%), and the LEW to increase by 0.06 m (a relative change of 120%).

#### 3) WAVEFORM RESULTS: KA HV
Before deconvolution, the SRP is located at a range of 1.78 m, with a power of −54 dB. The MSS is located at 1.59 m, with a power of −79 dB; resulting in a SFDR of 25 dBc. The WDP is located at 1.72 m, resulting in a LEW of 0.06 m.

After deconvolution, the SRP remains located at 1.78 m, with a power of −53 dB. The MSS shifts to 1.65 m, with a power of −91 dB; resulting in an increased SFDR of 38 dBc. The WDP is located at 1.70 m, giving an expanded LEW of 0.08 m. Deconvolution causes the SFDR to increase by 13 dB (a relative change of 52%), and the LEW to increase by 0.02 m (a relative change of 33%).

#### 4) WAVEFORM RESULTS: KU VV
Before deconvolution, the SRP is located at a range of 1.78 m, with a power of −18 dB. The MSS is located at 1.68 m, with a power of −54 dB; resulting in a SFDR of 36 dBc. The WDP is located at 1.70 m, resulting in a LEW of 0.08 m.

After deconvolution, the SRP is located at 1.79 m, with a power of −17 dB. The MSS shifts to 1.36 m, with a power of −80 dB; resulting in an increased SFDR of 63 dBc. The WDP is located at 1.51 m, giving an expanded LEW of 0.28 m. Deconvolution causes the SFDR to increase by 27 dB (a relative change of 75%), and the LEW to increase by 0.20 m (a relative change of 250%).

#### 5) WAVEFORM RESULTS: KU HV
Before deconvolution, the SRP is located at a range of 1.81 m, with a power of −49 dB.

After deconvolution, the SRP is located at 1.80 m with a power of −47 dB. The sidelobes appear indistinct, with little change in signal power observed before and after deconvolution.

### C. SHORT TIME OFFSET (NORTHERN TRANSECT)
This example is from the 16 January 2020, and represents a short, 8 day, offset from when the nonlinearities were characterized. The results presented in this section demonstrate the effectiveness of the deconvolution waveforms in a more typical use case of KuKa at MOSAiC: a stare mode transect over a well-developed snowpack on SYI [26], [27].

#### 1) ECHOGRAM RESULTS
Echograms showing subset of Northern transect data from the 16 January 2020 are shown in Fig. 10, this is the same Northern transect data as shown in S2020 (their figure 7 [26]).

The upper set of panels in Fig. 10 show the data before deconvolution. For Ka VV and Ku VV prominent surface returns are observed, but with strong diffuse radar returns observed at greater ranges. For Ka HV and Ku HV the surface returns are much less prominent, and more diffuse (compared to Ka VV and Ku VV). Distinct sidelobes are observed for Ka
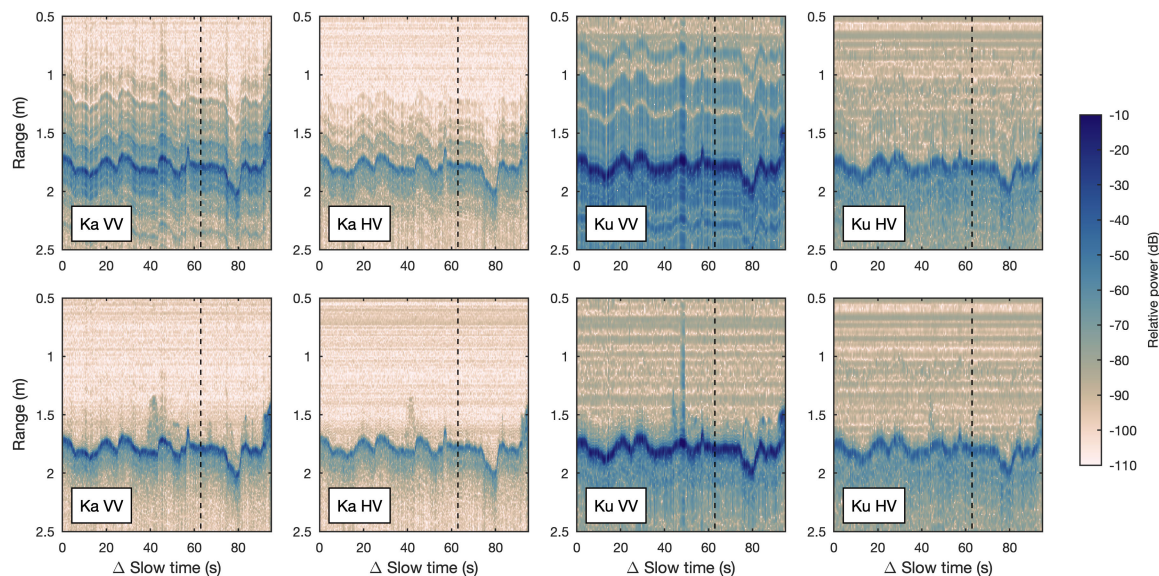
**FIGURE 8.** Echograms displaying a subset of lead transect data collected on the 24 January 2020. The upper set of panels display data before deconvolution and the lower set of panels display data after deconvolution. The black dashed line indicates the location of the waveform data shown in Fig. 9.
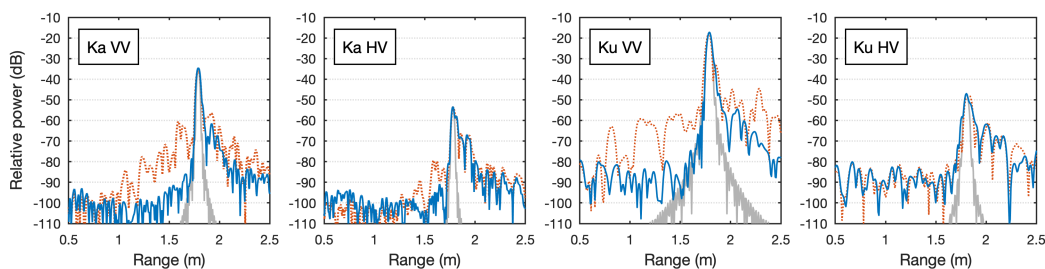


**FIGURE 9.** Waveforms corresponding to the black dashed lines in Fig. 8. The orange dotted line represents the data before deconvolution, the blue solid line represents the data after deconvolution, and the gray solid line illustrates the ideal point target response (represented by a Hann spectral window) that is colocated with the surface return peak, SRP.

VV and Ku VV; for Ka HV the sidelobes are indistinct and diffuse in character, and for Ku HV the sidelobes are obscured by the leakage signal.

From the lower set of panels in Fig. 10 we see that the application of the deconvolution waveforms has effectively suppressed the sidelobes for Ka VV, Ku VV and Ka HV. A large improvement in surface return clarity is observed for Ka HV making the unambiguous identification of the surface return much easier. Faint residual sidelobes at power levels similar to the noise floor are observed in the deconvolved data for Ka VV.

The black dashed line in Fig. 10 indicates the location of the waveforms shown in Fig. 11. We will describe the waveform results in the following section, and these results are also summarized in Table. 3.

### 2) WAVEFORM RESULTS: KA VV

Before deconvolution, the SRP (Surface Return Peak) is located at a range of 1.58 m, with a power of −31 dB. The

MSS (Maximum Spurious Signal) is located at 1.39 m, with a power of −56 dB; resulting in a SFDR (Spurious Free Dynamic Range) of 25 dBc. The WDP (Window Departure Point) is located at 1.53 m, resulting in a LEW (Leading Edge Width) of 0.05 m.

After deconvolution, the SRP remains located at 1.58 m, with a power of −30 dB. The MSS shifts to 1.40 m, with a power of −82 dB; resulting in an increased SFDR of 52 dBc. The WDP is located at 1.49 m, giving an expanded LEW of 0.09 m. Deconvolution causes the SFDR to increase by 27 dB (a relative change of 108%), and the LEW to increase by 0.04 m (a relative change of 80%).

### 3) WAVEFORM RESULTS: KA HV

Before deconvolution, the SRP is located at a range of 1.58 m, with a power of −62 dB. The MSS is located at 1.50 m, with a power of −77 dB; resulting in a SFDR of 15 dBc. The WDP is located at 1.55 m, resulting in a LEW of 0.03 m.
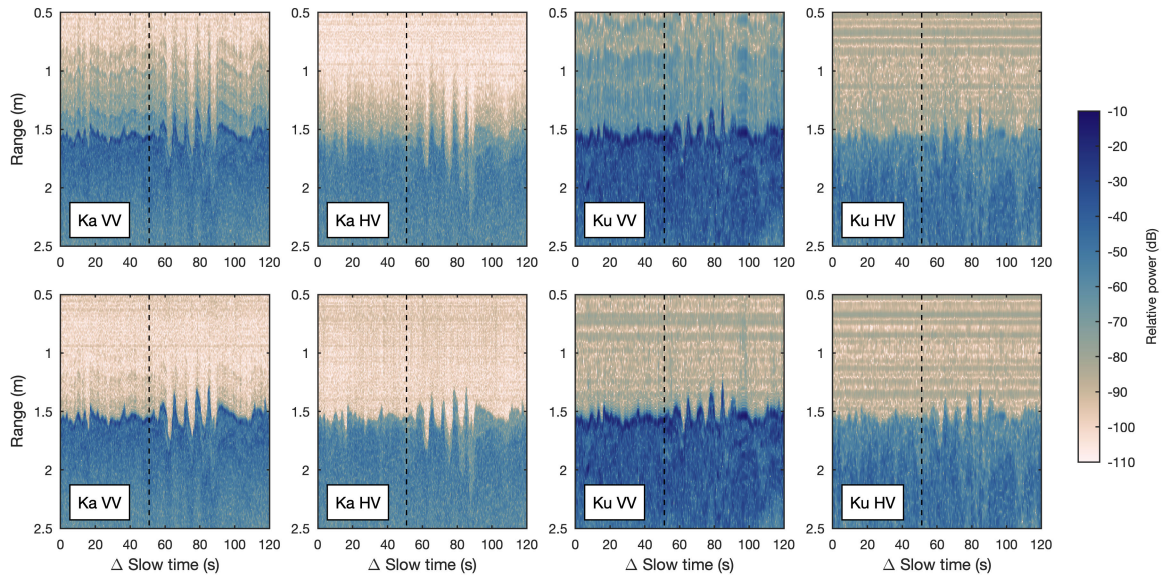
**FIGURE 10.** Echograms displaying a subset of Northern transect data collected on the 16 January 2020. The upper set of panels display data before deconvolution and the lower set of panels display data after deconvolution. The black dashed line indicates the location of the waveform data shown in Fig. 11.
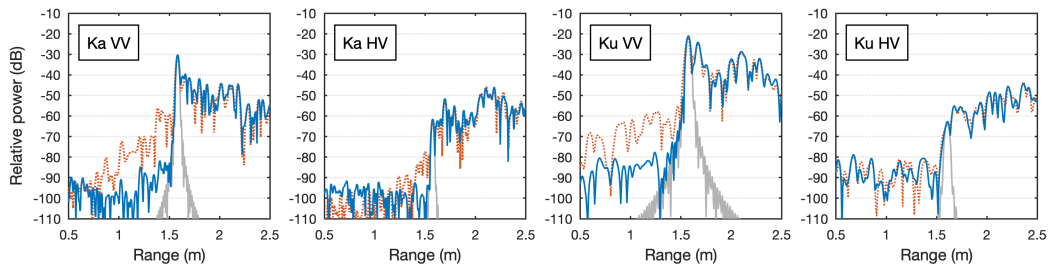


**FIGURE 11.** Waveforms corresponding to the black dashed line in Fig. 10. The orange dotted line represents the data before deconvolution, the blue solid line represents the data after deconvolution, and the gray solid line illustrates the ideal point target response (represented by a Hann spectral window) that is colocated with the surface return peak, SRP.

After deconvolution, the SRP is located at 1.57 m, with a power of −61 dB. The MSS shifts to 1.40 m, with a power of −92 dB; resulting in an increased SFDR of 31 dBc. The WDP is located at 1.51 m, giving an expanded LEW of 0.06 m. Deconvolution causes the SFDR to increase by 16 dB (a relative change of 107%), and the LEW to increase by 0.03 m (a relative change of 100%).

#### 4) WAVEFORM RESULTS: KU VV

Before deconvolution, the SRP is located at a range of 1.57 m, with a power of −22 dB. The MSS is located at 1.47 m, with a power of −55 dB; resulting in a SFDR of 33 dBc. The WDP is located at 1.49 m, resulting in a LEW of 0.08 m.

After deconvolution, the SRP remains located at 1.57 m, with a power of −21 dB. The MSS shifts to 1.24 m, with a power of −78 dB; resulting in an increased SFDR of 57 dBc. The WDP is located at 1.29 m, giving an expanded LEW of 0.28 m. Deconvolution causes the SFDR to increase by 24 dB (a relative change of 73%), and the LEW to increase by 0.20 m (a relative change of 250%).

#### 5) WAVEFORM RESULTS: KU HV

For Ku HV, before deconvolution, the SRP is located at a range of 1.61 m with a power of −64 dB.

After deconvolution, the SRP remains located at 1.60 m with a power of −63 dB. The sidelobes appear indistinct, with little change in signal power observed before and after deconvolution.

#### D. LONG TIME OFFSET (NORTHERN TRANSECT)

This final example is from the 14 November 2019, representing a long, 71 day, offset from when the nonlinearities were characterized. The results presented here again demonstrate the effectiveness of the deconvolution waveforms in the more typical use case of KuKa at MOSAiC: a transect over a well-developed snowpack on SYI [26], [27].

#### 1) ECHOGRAM RESULTS

Echograms showing a subset of Northern transect data from the 14 November 2019 are shown in Fig. 12. The upper set
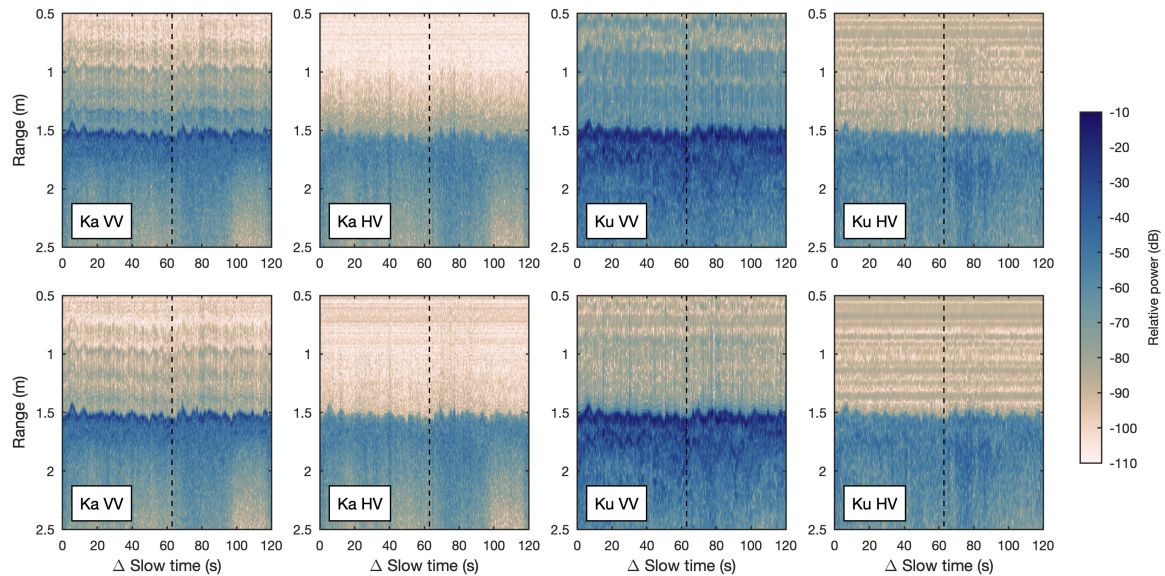
**FIGURE 12.** Echograms displaying a subset of Northern transect data collected on the 14 November 2019. The upper set of panels display data before deconvolution and the lower set of panels display data after deconvolution. The black dashed line indicates the location of the waveform data shown in Fig. 13.
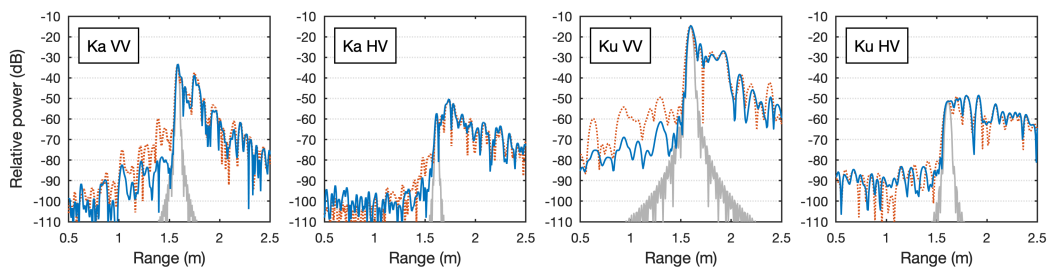


**FIGURE 13.** Waveforms corresponding to the black dashed line in Fig. 12. The orange dotted line represents the data before deconvolution, the blue solid line represents the data after deconvolution, and the gray solid line illustrates the ideal point target response (represented by a Hann spectral window) that is colocated with the surface return peak, SRP.

of panels in Fig. 12 displays the data prior to deconvolution. In the case of Ka VV and Ku VV, we observe prominent surface returns along with more diffuse radar returns at greater ranges. The surface returns for Ka HV and Ku HV are significantly less prominent and more diffuse compared to Ka VV and Ku VV. Distinct sidelobes are visible for Ka VV and Ku VV, while the sidelobes for Ka HV exhibit indistinct and diffuse characteristics. For Ku HV, the sidelobes are obscured by the leakage signal.

In the lower set of panels in Fig. 12, we see the data after applying deconvolution waveforms; from which we observe that deconvolution has only moderately suppressed the sidelobes. However, there is a noticeable improvement in the clarity of the surface return, particularly for Ka HV, making the unambiguous identification of the surface return easier. In the deconvolved data, residual sidelobes with powers greater than the noise floor are observed for Ka VV and Ku VV, while Ka HV exhibits residual sidelobes at power levels similar to the noise floor.

The black dashed line in Fig. 12 indicates the location of the waveforms shown in Fig. 13. We will describe the waveform results in the following section, and these results are also summarized in Table. 3.

### 2) WAVEFORM RESULTS: KA VV

Before deconvolution, the SRP (Surface Return Peak) is located at a range of 1.58 m, with a power of −34 dB. The MSS (Maximum Spurious Signal) is located at 1.39 m, with a power of −60 dB; resulting in a SFDR (Spurious Free Dynamic Range) of 26 dBc. The WDP (Window Departure Point) is located at 1.54 m, resulting in a LEW (Leading Edge Width) of 0.04 m.

After deconvolution, the SRP remains located at 1.58 m, with a power of −33 dB. The MSS shifts to 1.43 m, with a power of −78 dB; resulting in an increased SFDR of 45 dBc. The WDP is located at 1.51 m, giving an expanded LEW of 0.07 m. Deconvolution causes the SFDR to increase by

19 dB (a relative change of 73%), and the LEW to increase by 0.03 m (a relative change of 75%).

### 3) WAVEFORM RESULTS: KA HV

Before deconvolution, the SRP is located at a range of 1.61 m, with a power of −58 dB. The MSS is located at 1.55 m, with a power of −77 dB; resulting in a SFDR of 19 dBc. The WDP is located at 1.58 m, resulting in a LEW of 0.03 m.

After deconvolution, the SRP remains located at 1.61 m, with a power of −57 dB. The MSS shifts to 1.56 m, with a power of −84 dB; resulting in an increased SFDR of 27 dBc. The WDP is located at 1.56 m, giving an expanded LEW of 0.05 m. Deconvolution causes the SFDR to increase by 8 dB (a relative change of 42%), and the LEW to increase by 0.02 m (a relative change of 67%).

### 4) WAVEFORM RESULTS: KU VV

Before deconvolution, the SRP is located at a range of 1.60 m, with a power of −15 dB. The MSS is located at 1.30 m, with a power of −49 dB; resulting in a SFDR of 34 dBc. The WDP is located at 1.51 m, resulting in a LEW of 0.09 m.

After deconvolution, the SRP remains located at 1.60 m, with a power of −15 dB. The MSS shifts to 1.30 m, with a power of −61 dB; resulting in an increased SFDR of 46 dBc. The WDP is located at 1.38 m, giving an expanded LEW of 0.22 m. Deconvolution causes the SFDR to increase by 12 dB (a relative change of 35%), and the LEW to increase by 0.13 m (a relative change of 144%).

### 5) WAVEFORM RESULTS: KU HV

For Ku HV, before deconvolution, the SRP is located at a range of 1.61 m with a power of −51 dB.

After deconvolution, the SRP remains located at 1.61 m with a power of −51 dB. The sidelobes appear indistinct, with little change in signal power observed before and after deconvolution.

## VI. DISCUSSION

In this section, we will discuss how surface type affects the radar return and the changes to the echograms after deconvolution. We will then utilize the Spurious Free Dynamic Range (SFDR) to describe the changes in deconvolution performance over time, and the Leading Edge Width (LEW) to quantify the impact of deconvolution on surface return clarity.

### A. HOW SURFACE TYPE INFLUENCES THE RADAR RETURN AND SIDELOBE CHARACTERISTICS

In Section V, we presented deconvolution results for KuKa data collected on three different survey dates, and over two different surface types: the Lead transect and Northern transect. In this section, we will discuss how surface type affects the radar return and sidelobe characteristics, as well as the features that are observed after deconvolution.

### 1) LEAD TRANSECT

The results presented in Section V-B demonstrated the effectiveness of deconvolution waveforms on the specular radar returns collected during the KuKa lead transects (Section III-E). The lead surface consisted of nilas, characterized by high ice salinity and a significant coverage of frost flowers (Fig. 2). Although the surface roughness was not quantified, the presence of brine-enriched frost flowers likely made the surface too rough (at radar wavelengths) to generate phase-coherent returns, except in isolated cases. The strong dielectric boundary between the air and the highly saline nilas resulted in minimal radar penetration, leading to a highly prominent surface return peak, SRP. It is this single prominent SRP that produced the discrete sidelobes observed in the 20200124 Ka VV, Ka HV, and Ku VV data.

After deconvolution, faint diffuse radar returns were observed at greater ranges than the SRP for all bands and polarizations. Due to the strong dielectric boundary of the highly saline nilas, these returns cannot physically originate from beneath the ice surface. Therefore, we attribute the diffuse returns to off-nadir backscatter from radar-scale roughness elements on the nilas surface or the direct scattering from brine-enriched frost flowers. Further research is needed to investigate the effect of frost flowers on radar returns, especially in nadir-looking geometries; and this topic is briefly discussed in Section VII.

Faint above-surface features were also observed after deconvolution, particularly for Ka VV and Ka HV data (with their lower noise floor). As mentioned in Section IV-A, the lead surface return was observed to undulate between 1.5 and 2 meters (as KuKa is dragged along the lead edge); this was attributed to variations in the height of ice topography affecting the range between the KuKa antennas and the surface of the nilas (Section III-E). It is important to note that there were also lateral variations in KuKa's path during the lead transects, and the lead edge itself was not perfectly straight, with overhanging regions of ice jutting out over the lead surface. Therefore, the faint above-surface features can be attributed to these overhanging ice regions temporarily falling within the KuKa antenna beam pattern.

### 2) NORTHERN TRANSECTS

For the Northern transect results, presented in Section V-C and Section V-D, we demonstrated the effectiveness of deconvolution waveforms in the more typical use case of KuKa during MOSAiC, specifically in transects over a well-developed snowpack on SYI. The Northern transect snowpack was described in S2020 as dry, cold, brine-free, with a mean snow depth ranging between 24.2 and 26.7 cm (as measured from 2 to 30 January). Radar returns from the surface and within the snowpack depend strongly on its thermodynamic and geophysical properties, including snow depth, snow density/composition (wind slab or metamorphic snow), scatterer size, snow salinity, and temperature (in the case of saline snowpacks) [26].

**TABLE 3.** Summary of the results presented in Section V, showing the change in quantitative metrics before deconvolution, after deconvolution, and the difference (after - before) deconvolution.

| Parameter | 20200124 | | | 20200116 | | | 20191114 | | |
|---|---|---|---|---|---|---|---|---|---|
| | Ka VV | Ka HV | Ku VV | Ka VV | Ka HV | Ku VV | Ka VV | Ka HV | Ku VV |
| **Before deconvolution** | | | | | | | | | |
| Surface return peak range (m) | 1.79 | 1.78 | 1.78 | 1.58 | 1.58 | 1.57 | 1.58 | 1.61 | 1.60 |
| Window departure point (m) | 1.74 | 1.72 | 1.70 | 1.53 | 1.55 | 1.49 | 1.54 | 1.58 | 1.51 |
| Leading edge width (m) | 0.05 | 0.06 | 0.08 | 0.05 | 0.03 | 0.08 | 0.04 | 0.03 | 0.09 |
| Surface return peak power (dB) | -36 | -54 | -18 | -31 | -62 | -22 | -34 | -58 | -15 |
| Maximum spurious signal (dB) | -60 | -79 | -54 | -56 | -77 | -55 | -60 | -77 | -49 |
| Spurious free dynamic range (dBc) | 24 | 25 | 36 | 25 | 15 | 33 | 26 | 19 | 34 |
| **After deconvolution** | | | | | | | | | |
| Surface return peak range (m) | 1.79 | 1.78 | 1.79 | 1.58 | 1.57 | 1.57 | 1.58 | 1.61 | 1.60 |
| Window departure point (m) | 1.68 | 1.70 | 1.51 | 1.49 | 1.51 | 1.29 | 1.51 | 1.56 | 1.38 |
| Leading edge width (m) | 0.11 | 0.08 | 0.28 | 0.09 | 0.06 | 0.28 | 0.07 | 0.05 | 0.22 |
| Surface return peak power (dB) | -34 | -53 | -17 | -30 | -61 | -21 | -33 | -57 | -15 |
| Maximum spurious signal (dB) | -86 | -91 | -80 | -82 | -92 | -78 | -78 | -84 | -61 |
| Spurious free dynamic range (dBc) | 52 | 38 | 63 | 52 | 31 | 57 | 45 | 27 | 46 |
| **Change (after-before) deconvolution** | | | | | | | | | |
| Leading edge width, change (m) | 0.06 | 0.02 | 0.20 | 0.04 | 0.03 | 0.20 | 0.03 | 0.02 | 0.13 |
| Leading edge width, relative change (%) | 120 | 33 | 250 | 80 | 100 | 250 | 75 | 67 | 144 |
| Spurious free dynamic range, change (dB) | 28 | 13 | 27 | 27 | 16 | 24 | 19 | 8 | 12 |
| Spurious free dynamic range, relative change (%) | 117 | 52 | 75 | 108 | 107 | 73 | 73 | 42 | 35 |

In the case of the Northern transect data, we defined the SRP as the local peak originating from the air-snow interface at the top of the snowpack. For both Northern transect examples, the Ka VV and Ku VV data exhibited prominent SRPs, although with lower peak prominence compared to the lead transect data. Discrete sidelobes were observed for Ka VV and Ku VV, but they appeared more diffuse compared to the examples from the lead transect due to the lower prominence of the SRP. For Ka HV, the SRP was only weakly prominent or non-prominent, resulting in indistinct and diffuse sidelobes. The sidelobes from the strong snowpack returns combined with SRP sidelobes, and the surface return itself, to produce a gradual increase in power from the noise floor up to the air-snow interface return. This made it visually challenging to discern the leading edge of the SRP, especially for the 20200116 Ka HV data with its high-power snowpack returns.

The detailed analysis of the scattering properties of the MOSAiC snowpack, under differing environmental conditions, are described in recent KuKa papers [27], [66], [67].

## B. CHANGE IN DECONVOLUTION PERFORMANCE WITH TIME

In Section II-H, we noted that the potential drift of FMCW nonlinearities over time are attributed, in the literature, to temperature and power supply voltage variations [33], [34], [55]. Fig. 7 in Section IV-H showed small differences in the amplitude nonlinearities, $A_{\mathcal{E}}(t, \tau)$, and phase nonlinearities, $\phi_{\mathcal{E}}(t, \tau)$, despite the lead transect data being collected only a day apart.

In the results section (Section V), we presented echograms, and corresponding waveforms, for three different time offsets from the lead transects: zero time offset (Section V-B), short time offset (8 days) (Section V-C), and long time offset (71 days) (Section V-D). In this section, we discuss both the echograms and waveforms results to describe how deconvolution performance changes over time.

### 1) ECHOGRAMS

The echograms for 20200124, shown in Fig. 8, provide qualitative evidence that deconvolution effectively suppresses sidelobes in Ka VV, Ka HV, and Ku VV data. However, the improvement is only marginal for Ku HV due to the presence of the leakage signal. Deconvolution also revealed subtle near-surface features that were not initially visible in the original data (Section: VI-A).

In the 20200116 echograms, displayed in Fig. 10, deconvolution was also shown to successfully suppresses sidelobes in Ka VV, Ka HV, and Ku VV data. However, in the Ka VV echogram, faint residual sidelobes were observed at power levels similar to the noise floor, which were not visible in the 20200124 data. These faint residual sidelobes were absent in the Ka HV data due to the lower SRP power and prominence. Similarly, the residual sidelobes were also absent in the Ku VV and Ku HV data due to the presence of the enhanced leakage signal noise floor. The residual sidelobes could potentially be attributed to the influence of different surface types (Section VI-A), but they are more likely the result of a slight degradation in deconvolution performance in the 8 days between 20200124 and 20200116.

The 20191114 echograms, shown in Fig. 12, indicate that here deconvolution is significantly less effective in suppressing sidelobes compared to the 20200124 or 20200116 data. The residual sidelobes in Ka VV and Ku VV data appeared more pronounced and exhibited power levels higher than the noise floor, with the Ka HV data having residual sidelobes at power levels similar to the noise floor.

While the echograms provide a qualitative understanding of temporal changes in deconvolution effectiveness, we can further quantify and investigate these changes using the performance metrics introduced in Section V-A.

### 2) WAVEFORMS

The waveform results were discussed in Section V, and were also summarized in Table. 3. Deconvolution results in an almost 30 dB improvement in the spurious free dynamic range, SFDR; the maximum improvement for Ka VV, and Ku VV, is 28 dB and 27 dB, respectively, for the 20200124 data; the maximum improvement in the Ka HV data is 16 dB for the 20200116 data.

From Table. 3, we also observe that deconvolution typically increases the SRP power by 1-2 dB; with the origin of these changes related to the theory outlined in Section II-J. The nonlinearities increase the beat spectral bandwidth of the target response, causing target energy to spread into different frequencies and away from the beat frequency; deconvolution corrects the nonlinearities, bringing the target energy back towards the single beat frequency, and resulting in a slight increase in SRP power.

To further evaluate the variation in deconvolution effectiveness over time, we compare the results from 20200116 and 20191114, to those of 20200124. We calculate the change and relative change (as defined in (51)) by using the 20200124 SFDR values from Table. 3 as our reference values. These results are presented in Table. 4.

Compared to the 20200124 data, the SFDR values for 20200116 show a slight decrease of −1 dB for Ka VV, an increase of 3 dB for Ka HV, and a decrease of −3 dB for Ku VV. The increase in SFDR for the 20200116 Ka HV data may seem counterintuitive, but a closer examination of the corresponding Ka HV echograms reveals that the MSS in the 20200124 data is actually associated with a different leakage signal band compared to the 20200116 data. Specifically, the MSS for the 20200116 data is 1 dB lower than that of the 20200124 data, and the 20200116 data exhibited a pre-deconvolution MSS that is 2 dB higher than that of the 20200124 data, explaining the increase in SFDR. This example highlights an important point: that it is crucial to take into account variations in the noise floor and sidelobes (and refer to back to the echograms) when identifying the source of SFDR changes.

The SFDR values for 20191114 shows larger decreases of −9 dB for Ka VV, −5 dB for Ka HV, and −15 dB for Ku VV (compared to the 20200124 data). While there may be potential differences in snowpack properties between the 20200116 and 20191114 Northern transect

data, the decreased deconvolution performance is primarily responsible for the lower observed SFDR values.

From Table. 4, we can see that the deconvolution performance for the 20200116 data is thus similar to that of the 20200124 data, with a maximum change of −3 dB observed over the 8-day period between 20200124 and 20200116. However, the SFDR results demonstrate a decline in deconvolution performance of 8 dB for Ka VV and Ka HV, and 12 dB for Ku VV over the span of two months from 20200116 to 20191114. The most significant degradation in deconvolution performance occurs for Ku VV, with a 15 dB decrease in SFDR during the 71-day period between 20200124 and 20191114.

### 3) NONLINEARITY DRIFT WITH TIME

The changes in deconvolution performance, shown in Section VI-B1, and quantified in Section VI-B2, are due to the drift of FMCW nonlinearities over time. In general, anything that changes the (frequency-dependent) S-parameters of radar system components can potentially modify the nonlinearities (II-F and II-H).

For the KuKa radar system operating during MOSAiC, there are three main factors that are likely responsible for changes in the nonlinearities: mechanical shock/vibration during stare mode transects, the effect of repeated temperature cycling, and gradual hardware degradation due to the aging of KuKa system components.

During stare mode transects, such as the Northern transect, the KuKa radar system experiences vibrations, and discrete mechanical shocks, as it is pulled (on the transect sled) over regions of ice topography. These mechanical stresses can alter the alignment or functioning of sensitive RF components, and thus modify the existing nonlinearities.

As mentioned in S2020, the ambient air temperatures in the central Arctic can fluctuate significantly, even during the cold polar night, due to the effect of cyclone intrusions. From Fig 3 of S2020, the temperatures during the KuKa deployment at MOSAiC were observed to vary between −5 C and −35 C [26]. The KuKa RF units are insulated, and heated, to stabilize their internal temperatures in cold polar conditions; however, external RF components will still be exposed to these temperature changes. There are also the abrupt internal temperature changes that occur during the transition between scan and stare modes, during the time when the system is switched off and then restarted in the new mode. These repeated temperature cycling effects have the potential to cause subtle mechanical changes (such as thermal expansion and contraction) to KuKa radar external (and internal) RF components, also leading to the modification of nonlinearities.

The final factor is the gradual aging of KuKa radar system components, that occurs over much longer timescales. The aging of RF components is primarily due to the degradation of the transistors within the components [77]. Degradation in the chirp generator, such as the Linear FM synthesizer

**TABLE 4.** Comparison of deconvolution performance metrics between the different transect days.

| Parameter | 20200116 - 20200124 | | | 20191114 - 20200124 | | | 20191114 - 20200116 | | |
|---|---|---|---|---|---|---|---|---|---|
| | Ka VV | Ka HV | Ku VV | Ka VV | Ka HV | Ku VV | Ka VV | Ka HV | Ku VV |
| Leading edge width, relative change (%) | -40 | 67 | 0 | -45 | 33 | -106 | -5 | -33 | -106 |
| Spurious free dynamic range, change (dB) | -1 | 3 | -3 | -9 | -5 | -15 | -8 | -8 | -12 |

used in KuKa, can cause frequency shifts across its operating bandwidth; similarly, changes to the frequency-dependent gain profile of an LNA, can also change the location of the nonlinearities in the frequency domain.

The change in KuKa nonlinearities with time is due to the combination of all three factors. During continuous operation, during field campaigns such as MOSAiC, regular calibrations are required to counteract the effects of rough transects and temperature cycling. To obtain optimal performance calibration should occur before each transect, or at least on a weekly timescale. Calibration is also required after periods of inactivity and storage, due to more subtle temperature cycling effects, and the aging of KuKa RF components.

### C. HOW DECONVOLUTION IMPROVES SURFACE RETURN CLARITY

In Section VI-A, we discussed how surface type affects the radar return and sidelobe characteristics. In this section we further quantify the effect of deconvolution for Ka VV, Ka HV and Ku VV by discussing waveform changes in the context of the different surface types. Unfortunately the sidelobes for Ku HV are almost completely obscured by the leakage signal banding (that dominates the noise floor), with little change in signal power observed before and after deconvolution precluding a more detailed analysis of Ku HV.

The leading edge width, LEW, was defined in Section V-A as the range difference between the surface return peak, SRP, and the window departure point, WDP. The LEW can be used to quantify the clarity of the surface return, with larger LEW values indicating a less ambiguous surface return.

#### 1) KA VV

The deconvolution results for Ka VV are presented in Table 3. For the 20200124 lead transect data, deconvolution led to a LEW relative change of 120%. For the 20200116 Northern transect data, deconvolution resulted in a LEW relative change of 80%, while for the 20191114 Northern transect data, the LEW relative change was 75%.

When comparing the 20200116 data to the 20200124 data (Table 4), we see that despite their similar deconvolution performance (as described by a SFDR decrease of 1 dB), the LEW relative change value is actually 40% lower. Conversely, when comparing the 20191114 data to the 20200116 data, we see that despite having reduced deconvolution performance (as described by a SFDR decrease of 8 dB), the LEW relative change values are only 5% lower.

To understand these results, we must examine the ideal point target response in Figures 9, 11, and 13. We observe that

before deconvolution, the window departure point (WDP) for the 20200124, 20200116, and 20191114 data all occur on steep parts of the main lobe, with sidelobes decreasing in power from the MSS towards the WDP. The radar returns from within the snowpack for the 20200116 and 20191114 data alter the sidelobe characteristics and introduce additional phase noise to the SRP leading edge. This causes the post-deconvolution WDP (for the 20200116 and 20191114 data) to occur on a steeper part of the leading edge than the 20200124 data, explaining the observed reduction in the LEW relative change values. For the 20191114 data, the MSS after deconvolution is actually a residual sidelobe, but this is located far enough away from the main lobe to not overly influence the WDP. This explains the similar LEW relative change values despite the observed decrease in deconvolution performance.

These results also provide quantitative support for what we observed in the echograms; Due to the Ka VV downward-slanting sidelobe properties (Section VI-A), the surface returns were prominent and easily observable even before deconvolution, so the effect of deconvolution on Ka VV surface return clarity is modest.

#### 2) KA HV

The deconvolution results for Ka HV are also presented in Table 3. For the 20200124 lead transect data, deconvolution produced a LEW relative change of 33%. For the 20200116 Northern transect data, deconvolution led to a LEW relative change of 100%, while for the 20191114 Northern transect data, deconvolution yielded a LEW relative change of 67%.

Using the 20200124 Lead transect data as our reference dataset, we observe from Table 4 that the LEW relative change values are 67% higher for the 20200116 data and 33% higher for the 20191114 data; meaning that the LEW relative change value for the 20191114 data is 33% lower than that for the 20200116 data.

For Ka HV, both the 20200116 and 20191114 data exhibited greater LEW values, 67% and 33%, respectively, compared to the 20200124 data. Initially, this may appear counterintuitive, but it is a consequence of the differing sidelobe characteristics between the Northern transect and Lead transect data, as discussed in Section VI-A. The Ka HV 20200124 Lead transect data actually has similarities to the Ka VV 20200124 Lead transect data. In both cases, the SRP is the dominant return, with sidelobes that decrease in power from the MSS to the WDP. However, for the 20200116 and 20191114 Ka HV data, sidelobes

originating from strong snowpack returns combine with sidelobes from the less prominent SRP. This combination results in composite sidelobes that increase in power from the noise floor to the WDP, resulting in WDPs (and MSSs) that are closer to the SRP (i.e., on steeper parts of the main lobe) compared to the 20200124 data. After deconvolution, the WDPs for the 20200124 and 20200116 data are at the noise floor, while for the 20191114 data, the WDP remains on the steep part of the main lobe.

In summary, the composite sidelobes in the 20200116 and 20191114 data result in both upward-sloping sidelobes and higher power WDPs before deconvolution. This produces both the greater LEW relative change values and the observed large improvements in surface return clarity after deconvolution.

### 3) KU VV

The deconvolution results for Ku VV are displayed in Table 3. For the 20200124 lead transect data, deconvolution led to a 250% LEW relative change. Similarly, for the 20200116 Northern transect data, deconvolution also resulted in a 250% LEW relative change. However, for the 20191114 Northern transect data, deconvolution resulted in a 144% LEW relative change.

Using the 20200124 lead transect data as our reference dataset, we observe from Table 4 that the LEW relative change values remain the same for the 20200116 data but are 106% lower for the 20191114 data; meaning that the LEW relative change for the 20191114 data is also 106% lower than the 20200116 data.

In Table 3, we noted significantly higher LEW relative change values for Ku VV compared to Ka VV or Ka HV. This can be attributed to the prominent, higher-power Ku VV returns having more of the tapered (shallower) parts of their leading edges remaining above the noise floor after deconvolution, as shown by the point target response in Figures 9, 11, and 13. In Ku VV data, wide sidelobes are observed that increase in power towards the WDP (similar to the Ka HV case) whereas Ka VV had a dip in power towards the WDP. After deconvolution, the WDP for Ku VV occurs on the tapered parts of the main lobe, which are much further from the SRP than for the Ka-band data, thus explaining the significantly larger LEW relative change values.

From Table 3 and Table 4, we also note that, despite experiencing a reduction in SFDR value of −3 dB (20200116-20200124) and having different surface types, both the 20200116 and 20200124 Ku VV data share the same LEW relative change value of 250%. For both the 20200116 and 20200124 data, the SRPs are the dominant returns, even though there are strong returns from within the snowpack for the 20200116 data. The dominance of the 20200116 SRP, along with its high prominence, minimizes the influence of the snowpack returns on the SRP leading edge. Consequently, both the 20200124 and 20200116 data exhibit similar sidelobe characteristics before deconvolution, resulting in identical LEW values before and after deconvolution, and

thus the same relative change values (see Table 3). For the 20191114 data the influence of the higher residual sidelobes (due to decreased deconvolution performance) results in a WDP that, although still located on the tapered parts of the main lobe, is now closer to the SRP: explaining the observed LEW value reduction (relative to the 20200116 and 20200124 data).

## VII. CONCLUSION AND FUTURE WORK

This paper presented a practical approach to FMCW radar deconvolution, using data from the surface-based dual-frequency Ku- and Ka-band fully polarimetric radar (KuKa); collected during the 2019/2020 MOSAiC expedition.

An overview of the operating principles of FMCW radar, and the nonlinearities that cause sidelobes, were given in the background section. We then outlined the deployment of KuKa at MOSAiC, described the need for calibration, and introduced the lead transects as a method to obtain the KuKa impulse response. In the methodology section, we gave a detailed description of the steps needed to convert the KuKa impulse response into deconvolution waveforms, and the required methodology to apply the deconvolution waveforms to the whole KuKa MOSAiC dataset. In the results section, we introduced two metrics: the Spurious Free Dynamic Range (SFDR), to quantify how effective deconvolution is in suppressing sidelobes; and the Leading Edge Width (LEW), to quantify how effective deconvolution is in improving surface return clarity. We then presented results from KuKa stare mode transects over two different surface types, and three different offset dates: a zero-time offset (20200124) Lead transect dataset; and two Northern transect datasets over Second Year Ice (SYI): one with a short 8 day offset (20200116), and the other with a long 71 day offset (20191114). In the discussion section we used qualitative descriptions of example echograms, together with the SFDR and LEW, to describe: the effect of surface type on both the radar return and sidelobe characteristics, how deconvolution effectiveness changes with time, and finally the impact of deconvolution on surface return clarity.

We quantified the effects of deconvolution using sample waveforms from Ka VV, Ka HV and Ku VV data, but not for Ku HV due to the obscuring effect of the leakage signal on the sidelobes. The application of deconvolution waveforms resulted in an almost 30 dB improvement in the SFDR: the maximum improvement for Ka VV, and Ku VV, was 28 dB and 27 dB, respectively, for the 20200124 data; with a maximum improvement of 16 dB seen for the 20200116 Ka HV data. The SFDR results demonstrated that deconvolution performance degrades with offset time, a maximum degradation of −3 dB (Ku VV) was observed over the 8 days between 20200124 and 20200116; and a maximum degradation of −15 dB (Ku VV) over the 71 days, between 20200124 and 20191114; with an associated decline in deconvolution performance of 8 dB for Ka VV and Ka HV, and 12 dB for Ku VV observed over the two months from 20200116 to 20191114.

The LEW results showed that the influence of deconvolution on surface return clarity depends on a combination of factors such as: the shape of the sidelobes before deconvolution, the prominence of the surface return, the influence of snowpack returns, as well as the time-dependent reduction in deconvolution effectiveness. Deconvolution was shown to improve the surface return clarity for all data, but specifically for the Ka HV 20200116 and 20191114 data; where dominant returns from within the snowpack, produced sidelobes that sloped up to the main lobe from the noise floor, obscuring the surface return.

There is ample scope for future work, we have seen that if nonlinearities can be detected, i.e. if the sidelobes are not obscured by the leakage signal, then they can be successfully characterized and deconvolution waveforms created. The issue of leakage signal banding dominating the noise floor in Ku-band data, particularly for Ku HV datasets, needs to be addressed. Future modifications to the KuKa system hardware should focus on reducing the leakage signal, thereby improving the SNR of Ku-band data, allowing nonlinearities to be characterized. This improvement will aid in identifying low power returns (such as from low-density, fresh snow), and yield improved comparisons between Ka HV and Ku HV data.

As discussed in Section III-D, the metal plate used at MOSAiC proved to be an unsuitable calibration target for characterizing FMCW nonlinearities. In future KuKa campaigns a larger metal plate/sheet is required, with dimensions sufficient to contain the first Fresnel zone, beam-limited footprint, and pulse-limited footprint (at both Ka-band and Ku-band frequencies). From Section III-D, the maximum footprint size, at both Ka-band and Ku-band, corresponds to the pulse-limited footprint; the diameters of which are $F_{\text{Pulse}} = 55$ cm for Ka-band, and $F_{\text{Pulse}} = 71$ cm for Ku-band. In stare mode, there is also a 70 cm lateral separation between the Ka-band and Ku-band antennas; with an associated transmit-receive antenna spacing of 7.7 cm for Ka-band and 13.4 cm for Ku-band. Based upon these dimensions, any future metal plate should be at least $144 \times 77$ cm in size, in order to simultaneously accommodate both the Ka-band and Ku-band pulse-limited footprints. These dimensions are similar to standard US/Canadian door size of $203 \times 91$ cm, therefore a thin piece of sheet metal fixed to a flat standard door could provide a suitable bespoke calibration target.

The new calibration target design would provide radar returns free from off-nadir returns, and instead dominated by strong phase-coherent returns from within the first Fresnel zone; with an angular dependence of backscatter approaching that of a Dirac delta function. These strong coherent returns would minimize the need for averaging, quickly providing a highly accurate impulse response that can be used to generate high quality deconvolution waveforms. The effect of range on deconvolution effectiveness could then be explored systematically by raising the KuKa radar to different heights above the calibration target; and detailed investigation on the subtle temporal changes in nonlinearities would be possible through analysis of the changing impulse response throughout a campaign. Both experiments leading to enhanced understanding on the factors influencing the nonlinearities and further informing calibration strategies for future KuKa deployments.

In this paper, we also demonstrated that nilas can serve as a natural calibration target for obtaining the KuKa impulse response, when a suitable artificial calibration target is unavailable. Further research, under controlled conditions, is required to understand the effects of frost flowers on radar backscatter at normal incidence for Ka-band and Ku-band frequencies. Experiments, such as those conducted at the Sea ice mesocosm facility (SERF) [78], [79], could provide valuable insights into the impact of frost flowers at nadir scattering geometries. These experiments should involve imaging each KuKa footprint with both a camera and a Terrestrial Laser Scanning (TLS) system, to accurately characterize surface roughness. The combination of large metal sheet calibrations and frost flower experiments would allow for detailed investigations of the effects of frost flowers, and radar-scale roughness, on amplitude and phase nonlinearities across the entire FMCW frequency sweep.

During field campaigns, such as MOSAiC, regular calibrations are required to counteract the effects of rough transects and temperature cycling. To maintain optimal deconvolution effectiveness, and effective suppression of sidelobes, calibration should occur at least on a weekly timescale, and ideally before each KuKa transect. Calibration is also required after periods of inactivity and storage, due to more subtle temperature cycling effects, and the gradual aging of KuKa RF components.

In summary, we have outlined a practical approach to FMCW deconvolution in the Sea ice domain; the techniques outlined in this paper are equally applicable to similar instruments operating in other fields of Earth Science and beyond; with the increased usage of low-cost FMCW radar on novel remote sensing platforms, such as drones, a better understanding of FMCW nonlinearities, and how to correct for them, will remain of paramount importance in the future.

## DATA AVAILABILITY STATEMENT

data (Version v1). Zenodo. https://doi.org/10.5281/zenodo.
7967058.

## REFERENCES

[1] U. Nixdorf et al., "MOSAiC extended acknowledgement," Zenodo, Multidisciplinary Drifting Observatory Study Arctic Climate (MOSAiC) Consortium, Tech. Rep., 2021. [Online]. Available: https://zenodo.org/records/5541624

[2] M. Rantanen, A. Y. Karpechko, A. Lipponen, K. Nordling, O. Hyvärinen, K. Ruosteenoja, T. Vihma, and A. Laaksonen, "The Arctic has warmed nearly four times faster than the globe since 1979," *Commun. Earth Environ.*, vol. 3, no. 1, p. 168, Aug. 2022.

[3] M. Siegert, A. Atkinson, A. Banwell, M. Brandon, P. Convey, B. Davies, R. Downie, T. Edwards, B. Hubbard, G. Marshall, J. Rogelj, J. Rumble, J. Stroeve, and D. Vaughan, "The Antarctic peninsula under a 1.5°C global warming scenario," *Frontiers Environ. Sci.*, vol. 7, p. 102, Jun. 2019.

[4] D. Wingham, C. Francis, S. Baker, C. Bouzinac, D. Brockley, R. Cullen, P. de Chateau-Thierry, S. Laxon, U. Mallow, C. Mavrocordatos, L. Phalippou, G. Ratier, L. Rey, F. Rostan, P. Viau, and D. Wallis, "CryoSat: A mission to determine the fluctuations in earth's land and marine ice fields," *Adv. Space Res.*, vol. 37, no. 4, pp. 841–871, Jan. 2006.

[5] J. Verron, P. Sengenes, J. Lambin, J. Noubel, N. Steunou, A. Guillot, N. Picot, S. Coutin-Faye, R. Sharma, R. M. Gairola, D. V. A. R. Murthy, J. G. Richman, D. Griffin, A. Pascual, F. Rémy, and P. K. Gupta, "The SARAL/AltiKa altimetry satellite mission," *Mar. Geodesy*, vol. 38, no. sup1, pp. 2–21, Sep. 2015.

[6] C. Donlon, B. Berruti, A. Buongiorno, M.-H. Ferreira, P. Féménias, J. Frerick, P. Goryl, U. Klein, H. Laur, C. Mavrocordatos, J. Nieke, H. Rebhan, B. Seitz, J. Stroede, and R. Sciarra, "The global monitoring for environment and security (GMES) sentinel-3 mission," *Remote Sens. Environ.*, vol. 120, pp. 37–57, May 2012.

[7] D. G. Long, "Polar applications of spaceborne scatterometers," *IEEE J. Sel. Topics Appl. Earth Observ. Remote Sens.*, vol. 10, no. 5, pp. 2307–2320, May 2017.

[8] W. Dierking, "Sea ice monitoring by synthetic aperture radar," *Oceanography*, vol. 26, no. 2, pp. 100–111, Jun. 2013.

[9] N. Zakhvatkina, V. Smirnov, and I. Bychkova, "Satellite SAR data-based sea ice classification: An overview," *Geosciences*, vol. 9, no. 4, p. 152, Mar. 2019.

[10] H. D. Griffiths, "New ideas in FM radar," *Electron. Commun. Eng. J.*, vol. 2, no. 5, p. 185, 1990.

[11] M. I. Skolnik, *Introduction To Radar Systems*. Boston, MA, USA: McGraw-Hill, 2001.

[12] M. Jankiraman, *FMCW Radar Design*. Norwood, MA, USA: Artech House, 2018.

[13] T. Rink, P. Kanagaratnam, D. Braaten, T. Akins, and S. Gogineni, "A wideband radar for mapping near-surface layers in snow," in *Proc. IEEE Int. Symp. Geosci. Remote Sens.*, Jul. 2006, pp. 3655–3657.

[14] P. Kanagaratnam, T. Markus, V. Lytle, B. Heavey, P. Jansen, G. Prescott, and S. P. Gogineni, "Ultrawideband radar measurements of thickness of snow over sea ice," *IEEE Trans. Geosci. Remote Sens.*, vol. 45, no. 9, pp. 2715–2724, Sep. 2007.

[15] H.-P. Marshall and G. Koh, "FMCW radars for snow research," *Cold Regions Sci. Technol.*, vol. 52, no. 2, pp. 118–131, Apr. 2008.

[16] B. Panzer, C. Leuschen, A. Patel, T. Markus, and S. Gogineni, "Ultra-wideband radar measurements of snow thickness over sea ice," in *Proc. IEEE Int. Geosci. Remote Sens. Symp.*, Jul. 2010, pp. 3130–3133.

[17] D. Gomez-Garcia, F. Rodriguez-Morales, C. Leuschen, and S. Gogineni, "KU-band radar altimeter for surface elevation measurements in polar regions using a wideband chirp generator with improved linearity," in *Proc. IEEE Int. Geosci. Remote Sens. Symp.*, Jul. 2012, pp. 4617–4620.

[18] J. B. Yan, S. Gogineni, D. Braaten, J. Brozena, F. Rodriguez-Morales, and E. Arnold, "Ultra-wideband radars operating over the frequency range of 2–18 GHZ for measurements on terrestrial snow and ice," in *Proc. IEEE Int. Geosci. Remote Sens. Symp. (IGARSS)*, Jul. 2016, pp. 7078–7081.

[19] B. Panzer, D. Gomez-Garcia, C. Leuschen, J. Paden, F. Rodriguez-Morales, A. Patel, T. Markus, B. Holt, and P. Gogineni, "An ultra-wideband, microwave radar for measuring snow thickness on sea ice and mapping near-surface internal layers in polar firn," *J. Glaciol.*, vol. 59, no. 214, pp. 244–254, 2013.

[20] A. Patel, J. Paden, C. Leuschen, R. Kwok, D. Gomez-Garcia, B. Panzer, M. W. J. Davidson, and S. Gogineni, "Fine-resolution radar altimeter measurements on land and sea ice," *IEEE Trans. Geosci. Remote Sens.*, vol. 53, no. 5, pp. 2547–2564, May 2015.

[21] S. Gogineni, J.-B. Yan, D. Gomez-Garcia, F. Rodriguez-Morales, C. Leuschen, Z. Wang, J. Paden, R. Hale, E. Arnold, and D. Braaten, "Ultra-wideband radars for measurements over ICE and SNOW," in *Proc. IEEE Int. Geosci. Remote Sens. Symp. (IGARSS)*, Jul. 2015, pp. 4204–4207.

[22] J.-B. Yan, S. Gogineni, F. Rodriguez-Morales, D. Gomez-Garcia, J. Paden, J. Li, C. J. Leuschen, D. A. Braaten, J. A. Richter-Menge, S. L. Farrell, J. Brozena, and R. D. Hale, "Airborne measurements of snow thickness: Using ultrawide-band frequency-modulated-continuous-wave radars," *IEEE Geosci. Remote Sens. Mag., Replaces Newsletter*, vol. 5, no. 2, pp. 57–76, Jun. 2017.

[23] J.-B. Yan, D. G.-G. Alvestegui, J. W. McDaniel, Y. Li, S. Gogineni, F. Rodriguez-Morales, J. Brozena, and C. J. Leuschen, "Ultrawideband FMCW radar for airborne measurements of snow over sea ice and land," *IEEE Trans. Geosci. Remote Sens.*, vol. 55, no. 2, pp. 834–843, Feb. 2017.

[24] J. A. MacGregor et al., "The scientific Legacy of NASA's operation icebridge," *Rev. Geophys.*, vol. 59, no. 2, 2021, Art. no. e2020RG000712.

[25] M. Nicolaus et al., "Overview of the MOSAiC expedition: Snow and sea ice," *Elem. Sci. Anth.*, vol. 10, no. 1, p. 46, 2022.

[26] J. Stroeve, V. Nandan, R. Willatt, R. Tonboe, S. Hendricks, R. Ricker, J. Mead, R. Mallett, M. Huntemann, P. Itkin, M. Schneebeli, D. Krampe, G. Spreen, J. Wilkinson, I. Matero, M. Hoppmann, and M. Tsamados, "Surface-based Ku- and Ka-band polarimetric radar for sea ice studies," *Cryosphere*, vol. 14, no. 12, pp. 4405–4426, Dec. 2020.

[27] R. Willatt et al., "Retrieval of snow depth on Arctic Sea ice from surface-based, polarimetric, dual-frequency radar altimetry," *Geophys. Res. Lett.*, vol. 50, no. 20, 2023, Art. no. e2023GL104461.

[28] A. Meta, P. Hoogeboom, and L. Ligthart, "Range non-linearities correction in FMCW SAR," in *Proc. IEEE Int. Symp. Geosci. Remote Sens.*, Jul. 2006, pp. 403–406.

[29] S. Ayhan, S. Scherr, A. Bhutani, B. Fischbach, M. Pauli, and T. Zwick, "Impact of frequency ramp nonlinearity, phase noise, and SNR on FMCW radar accuracy," *IEEE Trans. Microw. Theory Techn.*, vol. 64, no. 10, pp. 3290–3301, Oct. 2016.

[30] Y. Li, W. Hu, X. Zhang, Y. Zhao, J. Ni, and L. P. Ligthart, "A non-linear correction method for terahertz LFMCW radar," *IEEE Access*, vol. 8, pp. 102784–102794, 2020.

[31] H. Griffiths, "The effect of phase and amplitude errors in FM radar," in *Proc. IEE Colloq. High Time-Bandwidth Product Waveforms Radar Sonar*, 1991, pp. 1–9.

[32] P. J. Burke, "Ultra-linear chirp generation via VCO tuning predistortion," in *IEEE MTT-S Int. Microw. Symp. Dig.*, Jun. 1994, pp. 957–960.

[33] S. O. Piper, "Homodyne FMCW radar range resolution effects with sinusoidal nonlinearities in the frequency sweep," in *Proc. Int. Radar Conf.*, May 1995, pp. 563–567.

[34] M. Vossiek, P. Heide, M. Nalezinski, and V. Magori, "Novel FMCW radar system concept with adaptive compensation of phase errors," in *Proc. 26th Eur. Microw. Conf.*, Oct. 1996, pp. 135–139.

[35] T. Newman, S. L. Farrell, J. Richter-Menge, L. N. Connor, N. T. Kurtz, B. C. Elder, and D. McAdoo, "Assessment of radar-derived snow depth over Arctic sea ice," *J. Geophys. Res., Oceans*, vol. 119, no. 12, pp. 8578–8602, 2014.

[36] R. Kwok and C. Haas, "Effects of radar side-lobes on snow depth retrievals from operation icebridge," *J. Glaciol.*, vol. 61, no. 227, pp. 576–584, 2015.

[37] R. Kwok, N. T. Kurtz, L. Brucker, A. Ivanoff, T. Newman, S. L. Farrell, J. King, S. Howell, M. A. Webster, J. Paden, C. Leuschen, J. A. MacGregor, J. Richter-Menge, J. Harbeck, and M. Tschudi, "Intercomparison of snow depth retrievals over Arctic sea ice from radar data acquired by operation IceBridge," *Cryosphere*, vol. 11, no. 6, pp. 2571–2593, Nov. 2017.

[38] S. O. Piper, "Receiver frequency resolution for range resolution in homodyne FMCW radar," in *Proc. Nat. Telesyst. Conf.*, 1993, pp. 169–173.

[39] H. D. Griffiths and W. J. Bradford, "Digital generation of high time-bandwidth product linear FM waveforms for radar altimeters," *IEE Proc. F Radar Signal Process.*, vol. 139, no. 2, p. 160, 1992.

[40] A. Stove, "Modern FMCW radar—Techniques and applications," in *Proc. 1st Eur. Radar Conf. (EURAD)*, 2004, pp. 149–152.

[41] P. Wang, D. Millar, K. Parsons, and P. V. Orlik, "Nonlinearity correction for range estimation in FMCW millimeter-wave automotive radar," in *IEEE MTT-S Int. Microw. Symp. Dig.*, May 2018, pp. 1–3.

[42] K. B. Cooper, R. J. Dengler, N. Llombart, B. Thomas, G. Chattopadhyay, and P. H. Siegel, "THz imaging radar for standoff personnel screening," *IEEE Trans. THz Sci. Technol.*, vol. 1, no. 1, pp. 169–182, Sep. 2011.

[43] F. J. Harris, "On the use of windows for harmonic analysis with the discrete Fourier transform," *Proc. IEEE*, vol. 66, no. 1, pp. 51–83, Jan. 1978.

[44] A. Nuttall, "Some windows with very good sidelobe behavior," *IEEE Trans. Acoust., Speech, Signal Process.*, vol. ASSP-29, no. 1, pp. 84–91, Feb. 1981.

[45] R. G. Lyons, *Understanding Digital Signal Processing*. Upper Saddle River, NJ, USA: Prentice-Hall, 2011.

[46] A. G. Stove, "Linear FMCW radar techniques," *IEE Proc. F Radar Signal Process.*, vol. 139, no. 5, p. 343, 1992.

[47] K. Siddiq, R. J. Watson, S. R. Pennock, P. Avery, R. Poulton, and B. Dakin-Norris, "Phase noise analysis in FMCW radar systems," in *Proc. Eur. Microw. Conf. (EuMC)*, Sep. 2015, pp. 1523–1526.

[48] K. Siddiq, M. K. Hobden, S. R. Pennock, and R. J. Watson, "Phase noise in FMCW radar systems," *IEEE Trans. Aerosp. Electron. Syst.*, vol. 55, no. 1, pp. 70–81, Feb. 2019.

[49] G. M. Brooker, "Understanding millimetre wave FMCW radars," in *Proc. 1st Int. Conf. Sens. Technol.*, Palmerston North, New Zealand, 2005, pp. 1–6.

[50] M. C. Budge and M. P. Burt, "Range correlation effects on phase and amplitude noise," in *Proc. Southeastcon 93*, 1993, p. 5.

[51] K. Kurokawa, "Power waves and the scattering matrix," *IEEE Trans. Microw. Theory Techn.*, vol. MTT-13, no. 2, pp. 194–202, Mar. 1965.

[52] A. Ferrero and M. Pirola, "Generalized mixed-mode S-parameters," *IEEE Trans. Microw. Theory Techn.*, vol. 54, no. 1, pp. 458–463, Jan. 2006.

[53] Q. Yuan, "S-parameters for calculating the maximum efficiency of a MIMO-WPT system: Applicable to near/far field coupling, capacitive/magnetic coupling," *IEEE Microw. Mag.*, vol. 24, no. 4, pp. 40–48, Apr. 2023.

[54] S. Yamada, O. Boric-Lubecke, and V. M. Lubecke, "Cancellation techniques for LO leakage and DC offset in direct conversion systems," in *IEEE MTT-S Int. Microw. Symp. Dig.*, Jun. 2008, pp. 1191–1194.

[55] Z. Zhu, W. Yu, X. Zhang, and X. Qiu, "A correction method for distortions in FM-CW imaging system," in *Proc. IEEE Nat. Aerosp. Electron. Conf. NAECON*, vol. 1, Jun. 1996, pp. 323–326.

[56] A. Meta, P. Hoogeboom, and L. P. Ligthart, "Signal processing for FMCW SAR," *IEEE Trans. Geosci. Remote Sens.*, vol. 45, no. 11, pp. 3519–3532, Nov. 2007.

[57] G. Rubio-Cidre, A. Badolato, L. Úbeda-Medina, J. Grajal, B. Mencia-Oliva, and B.-P. Dorta-Naranjo, "DDS-based signal-generation architecture comparison for an imaging radar at 300 GHz," *IEEE Trans. Instrum. Meas.*, vol. 64, no. 11, pp. 3085–3098, Nov. 2015.

[58] J. Grajal, A. Badolato, G. Rubio-Cidre, L. Úbeda-Medina, B. Mencia-Oliva, A. Garcia-Pino, B. Gonzalez-Valdes, and O. Rubiños, "3-D high-resolution imaging radar at 300 GHz with enhanced FoV," *IEEE Trans. Microw. Theory Techn.*, vol. 63, no. 3, pp. 1097–1107, Mar. 2015.

[59] J. D. Park and W. J. Kim, "An efficient method of eliminating the range ambiguity for a low-cost FMCW radar using VCO tuning characteristics," *IEEE Trans. Microw. Theory Techn.*, vol. 54, no. 10, pp. 3623–3629, Oct. 2006.

[60] Y. Jiang, B. Deng, H. Wang, Y. Qin, and K. Liu, "An effective naonlinear phase compensation method for FMCW terahertz radar," *IEEE Photon. Technol. Lett.*, vol. 28, no. 15, pp. 1684–1687, Aug. 1, 2016.

[61] B. Mencia-Oliva, J. Grajal, O. A. Yeste-Ojeda, G. Rubio-Cidre, and A. Badolato, "Low-cost CW-LFM radar sensor at 100 GHz," *IEEE Trans. Microw. Theory Techn.*, vol. 61, no. 2, pp. 986–998, Feb. 2013.

[62] D. A. Robertson, S. L. Cassidy, and D. R. Bolton, "Nonlinearity and phase noise effects in 340 GHz 3D imaging radar," *Proc. SPIE*, vol. 8715, pp. 163–172, May 2013.

[63] R. J. C. Middleton, D. G. Macfarlane, and D. A. Robertson, "Range autofocus for linearly frequency-modulated continuous wave radar," *IET Radar, Sonar Navigat.*, vol. 5, no. 3, pp. 288–295, Mar. 2011.

[64] J. Yang, C. Liu, and Y. Wang, "Nonlinearity correction of FMCW SAR based on homomorphic deconvolution," *IEEE Geosci. Remote Sens. Lett.*, vol. 10, no. 5, pp. 991–995, Sep. 2013.

[65] A. Anghel, G. Vasile, R. Cacoveanu, C. Ioana, and S. Ciochina, "Short-range wideband FMCW radar for millimetric displacement measurements," *IEEE Trans. Geosci. Remote Sens.*, vol. 52, no. 9, pp. 5633–5642, Sep. 2014.

[66] J. Stroeve et al., "Rain on snow (ROS) understudied in sea ice remote sensing: A multi-sensor analysis of ROS during MOSAiC (Multidisciplinary drifting observatory for the study of Arctic Climate)," *Cryosphere*, vol. 16, no. 10, pp. 4223–4250, Oct. 2022.

[67] V. Nandan et al., "Wind redistribution of snow impacts the Ka- and Ku-band radar signatures of Arctic sea ice," *Cryosphere*, vol. 17, no. 6, pp. 2211–2229, Jun. 2023.

[68] R. N. Bracewell, *The Fourier Transform and Its Applications*. New York, NY, USA: McGraw-Hill, 2000.

[69] M. A. Richards, *Fundamentals of Radar Signal Processing*, 2nd ed., New York, NY, USA: McGraw-Hill, 2014.

[70] D. B. Chelton, E. J. Walsh, and J. L. MacArthur, "Pulse compression and sea level tracking in satellite altimetry," *J. Atmos. Ocean. Technol.*, vol. 6, no. 3, pp. 407–438, Jun. 1989.

[71] R. K. Raney, "The delay/Doppler radar altimeter," *IEEE Trans. Geosci. Remote Sens.*, vol. 36, no. 5, pp. 1578–1588, May 1998.

[72] D. B. Chelton, J. C. Ries, B. J. Haines, L.-L. Fu, and P. S. Callahan, "Satellite altimetry," in *Satellite Altimetry and Earth Sciences-A Handbook of Techniques and Applications* (International Geophysics). Amsterdam, The Netherlands: Elsevier, 2001, ch. 1, p. 1.

[73] W. F. Weeks and S. F. Ackley, "The growth, structure, and properties of sea ice," in *The Geophysics of Sea Ice*. Boston, MA, USA: Springer, 1986, pp. 9–164.

[74] I. Allison, R. E. Brandt, and S. G. Warren, "East Antarctic sea ice: Albedo, thickness distribution, and snow cover," *J. Geophys. Res., Oceans*, vol. 98, no. 7, pp. 12417–12429, Jul. 1993.

[75] D. K. Perovich and J. A. Richter-Menge, "Surface characteristics of lead ice," *J. Geophys. Res., Oceans*, vol. 99, no. 8, pp. 16341–16350, Aug. 1994.

[76] R. W. Style and M. G. Worster, "Frost flower formation on sea ice and lake ice," *Geophys. Res. Lett.*, vol. 36, no. 11, pp. 1–4, Jun. 2009.

[77] T. D. Ridder and R. M. Narayanan, "Total reliability of radar systems: Incorporating component degradation effects in operational reliability," *Proc. SPIE*, vol. 11003, pp. 270–279, May 2019.

[78] D. Isleifson, R. J. Galley, D. G. Barber, J. C. Landy, A. S. Komarov, and L. Shafai, "A study on the C-band polarimetric scattering and physical characteristics of frost flowers on experimental sea ice," *IEEE Trans. Geosci. Remote Sens.*, vol. 52, no. 3, pp. 1787–1798, Mar. 2014.

[79] D. Isleifson, R. J. Galley, N. Firoozy, J. C. Landy, and D. G. Barber, "Investigations into frost flower physical characteristics and the C-band scattering response," *Remote Sens.*, vol. 10, no. 7, p. 991, Jun. 2018.

**THOMAS NEWMAN** received the M.Sci. degree in earth and space science and the Ph.D. degree in earth sciences from University College London, London, U.K., in 2006 and 2011, respectively.

From 2011 to 2016, he was a Research Associate with the Earth System Science Interdisciplinary Center (ESSIC), University of Maryland. From 2017 to 2018, he was a Research Fellow with the Department of Physics, University of Toronto. While in North America, he collaborated with both U.S. and Canadian government agencies on their Arctic science programs and field campaigns including: National Oceanic and Atmospheric Administration (NOAA), National Aeronautics and Space Administration (NASA), U.S. Naval Research Laboratory (NRL), and Environment and Climate Change Canada (ECCC). Since 2019, he has been a Research Fellow with the Centre for Polar Observation and Modelling, Department of Earth Sciences, University College London. His research interests include sea ice remote sensing and validation survey design, radar forward-modelling and backscatter simulation, wavelet-based signal and image processing, snow bedform dynamics, surface roughness characterization, fractals and complexity theory, and drone applications for polar science.

**JULIENNE C. STROEVE** received the Ph.D. degree in geography from the University of Colorado Boulder, in 1996, for her work in understanding Greenland climate variability. Afterwards, she became a Senior Research Scientist with the National Snow and Ice Data Center (NSIDC), Cooperative Institute for Research in Environmental Sciences (CIRES), CU-Boulder. In 2016, she moved to University College London. In 2018, she was awarded a Canada 150 Excellence Research Chair with the University of Manitoba. In 2023, she was awarded a Helmholtz Fellowship with the Alfred Wegener Institute. Her Arctic research interests include remote sensing of snow and ice, sea ice forecasting at various time-scales, climate change, and impacts of sea ice loss on marine ecosystems and native communities. She has participated in several field campaigns in Greenland and the Arctic Ocean, including the year-long German-led MOSAiC expedition, in 2019 and 2020. She is also a Science Advisor of Arctic Basecamp, a non-profit that brings the urgency of Arctic change to policy makers and industry leaders at the World Economic Forum each year.

**VISHNU NANDAN** received the M.Sc. degree in earth observation sciences from ITC, The Netherlands, in 2012, and the Ph.D. degree in physical geography from the University of Calgary, Canada, in 2018. He is currently a Sea Ice Geophysical Field Scientist specialized in polarimetric radar remote sensing of Arctic and Antarctic sea ice. His research interests include using multi-frequency surface-based radar altimeters and scatterometers to quantify the impact of Snow and their geophysical properties on the accuracy of snow depth and sea ice thickness estimates. He works with Amrita University, India, as an Assistant Professor.

**ROSEMARY C. WILLATT** received the M.Sci. degree in astronomy and the Ph.D. degree in geophysics from University College London, London, U.K., in 2006 and 2012, respectively. She is currently a Lecturer and the Climate Lead of the UCL Department of Earth Sciences and the Principal Investigator for Sea Ice Earth Observation with the Centre for Polar Observation and Modelling (CPOM). She has investigated radar interaction with snow-covered sea ice for several years, including experiments in the Arctic, Antarctic, and laboratory settings. Her work includes studies at a range of scales from microstructure, surface-based, airborne, and satellite studies to explore how physical snow characteristics affect radar scattering. She has also led a number of equality, diversity, and inclusion initiatives in science.

**JAMES B. MEAD** (Senior Member, IEEE) received the B.S.E.E. degree from the University of Virginia, Charlottesville, in 1981, and the Ph.D. degree from the University of Massachusetts, Amherst, in 1989. From 1981 to 1986, he was with the Singer Kearfott Division, Wayne, NJ, USA, where he designed microstrip and leaky wave antennas for Doppler navigation systems. In June 1986, he joined the Microwave Remote Sensing Laboratory, University of Massachusetts, where his graduate work involved the development of millimeter-wave polarimetric radars at 95 and 225 GHz and the use of millimeter-wave radars for cloud research. From 1990 to 1996, he was employed by the University of Massachusetts, where he was a Senior Research Fellow and later a Research Associate Professor. His research interests include radar polarimetry and the development of digital beamforming radar systems for atmospheric and oceanographic applications. Since 1996, he has been the President of ProSensing Inc., which specializes in custom radar and radiometer systems for environmental remote sensing applications.

**ROBBIE MALLETT** received the bachelor's degree in physics from the University of Oxford, U.K., in 2016, the M.Sc. degree in climate change from UCL, U.K., in 2018, and the Ph.D. degree from the UCL's Centre for Polar Observation and Modelling, in 2022, combining field campaigns in both polar regions with satellite observations and computer modeling approaches.

In 2023, he joined the University of Manitoba, Canada, and returned to Antarctica, overwintering for eight months with Rothera research station. He is currently with the Earth Observation Group, UiT The Arctic University of Norway. He is a fellow of the International Arctic Science Committee.

**MICHEL TSAMADOS** received the M.S. degree in statistical physics from the École Normale Supérieure de Lyon, Lyon, France, in 2005, and the Ph.D. degree in theoretical physics from the Université Claude Bernard, Villeurbanne, France, in 2009, with a focus on the mechanical response of glassy materials from a theoretical and modeling perspective. He held several postdoctoral research positions with the Centre for Polar Observations and Modeling, University College London, London, U.K., and the University of Reading, U.K., where he implemented several new sea ice model parameterizations including a new anisotropic rheology and a new form drag formulation into the Los Alamos CICE sea ice model. Since 2014, he has been a Lecturer and currently an Associate Professor with the Department of Earth Sciences, UCL, where he was involved in the development and analysis of several satellite products in the polar regions ranging from sea ice thickness, sea surface elevation, significant wave heights, snow on sea ice, sea ice roughness, and melt pond concentration. He is also driving several AI related initiatives as the Head of Theme of the Space Domain with UCL, as a the Met Office Academic Partnership working group lead on data science for climate and the environment for and as an UCL ESA Laboratory PI. He is also providing regular expertise on several polar satellite mission (e.g., SKIM and CRISTAL). He received the Prestigious Agrégation de Physique from the École Normale Supérieure de Lyon, in 2004.

**MARCUS HUNTEMANN** received the Diploma (M.Sc.) degree in physics from the University of Bremen, Bremen, Germany, in 2011, and the Ph.D. degree, in 2015, on low frequency microwave remote sensing of sea ice thickness from satellite observations. He continued his studies as a Postdoctoral Researcher with the Alfred Wegener Institute for Polar and Marine Research and the Institute of Environmental Physics, University of Bremen, and worked on the development and validation of sea ice emissivity and scattering models. Furthermore, he has participated in several field campaigns in the Polar regions, including the MOSAiC expedition, where he maintained parts of the remote sensing site, where the KuKa instrument was installed. His current research interest includes consistent retrieval of multiple parameters from passive microwave remote sensing data.

**STEFAN HENDRICKS** received the Ph.D. degree from the University of Bremen, Bremen, Germany, in 2009. Besides the Ph.D. Program, he was a Project Scientist and nowadays as a Senior Scientist with the Sea Ice Physics Section, Alfred Wegener Institute, Helmholtz Centre for Polar and Marine Research, Bremerhaven. His research interests include observation of global sea-ice thickness with geophysical methods and satellite remote sensing.

**RASMUS T. TONBOE** received the M.Sc. degree in geology from the University of Aarhus, in 1997, and the Ph.D. degree in geophysics from the University of Copenhagen, Denmark, in 2004. He is currently an Associate Professor with the Technical University of Denmark, Copenhagen. His research interests include microwave and infrared remote sensing of sea ice in particular modeling of thermal emission and backscatter from sea ice and the use of forward model inversion for estimating sea ice snow cover, and other properties. He has field work experience, operating radiometers in the field, snow and sea ice sampling, and installing meteorological monitoring stations on sea ice. He is a member of ESA's MetOp SG MWI and ICI Science Advisory Group and the ESA CIMR Mission Advisory Group.

• • •

**GUNNAR SPREEN** received the Diploma (M.Sc.) degree in physics and the Ph.D. degree in oceanography from the University of Hamburg, Hamburg, Germany, in 2004 and 2008, respectively. He works on satellite remote sensing of polar regions with a focus on monitoring changes of sea ice (extent, mass, and dynamics) and on understanding underlying climate processes. Satellite measurements are evaluated using ground-based and airborne field observations. He is currently the Head of the Research Group "Remote Sensing of Polar Regions," University of Bremen, Institute of Environmental Physics, Bremen, Germany. Before, he was a Research Scientist with Norwegian Polar Institute, Tromsø, Norway, and a Postdoctoral Scholar with the Jet Propulsion Laboratory, California Institute of Technology, Pasadena, CA, USA. His current work addresses the development of new retrievals for sea ice parameters for upcoming satellite microwave radiometer and radar missions and data analysis from the international Arctic drift expedition MOSAiC.